JGR Planets

RESEARCH ARTICLE
10.1029/2021JE007079

Special Section:
ExoMars Trace Gas Orbiter - One Martian Year of Science

Explaining NOMAD D/H Observations by Cloud-Induced Fractionation of Water Vapor on Mars

F. Daerden[1], L. Neary[1], G. Villanueva[2], G. Liuzzi[2,3], S. Aoki[1,4], R. T. Clancy[5], J. A. Whiteway[6], B. J. Sandor[5], M. D. Smith[2], M. J. Wolff[5], A. Pankine[5], A. Khayat[2], R. Novak[7], B. Cantor[8], M. Crismani[9], M. J. Mumma[2], S. Viscardy[1], J. Erwin[1], C. Depiesse[1], A. Mahieux[1], A. Piccialli[1], S. Robert[1], L. Trompet[1], Y. Willame[1], E. Neefs[1], I. R. Thomas[1], B. Ristic[1], and A. C. Vandaele[1]

[1]Royal Belgian Institute for Space Aeronomy (BIRA-IASB), Brussels, Belgium, [2]NASA Goddard Space Flight Center, Greenbelt, MD, USA, [3]Department of Physics, School of Arts and Sciences, American University, Washington, DC, USA, [4]Institute of Space and Astronautical Science (ISAS), Japan Aerospace Exploration Agency (JAXA), Sagamihara, Japan, [5]Space Science Institute, Boulder, CO, USA, [6]Centre for Research in Earth and Space Science, York University, Toronto, ON, Canada, [7]Iona College, New Rochelle, NY, USA, [8]Malin Space Science Systems, San Diego, CA, USA, [9]California State University, San Bernardino, CA, USA

Key Points:

- Hydrogen fractionation by clouds in Mars water vapor is simulated and evaluated with NOMAD D/H observations in and out of dust storms
- The model D/H ratio is constant and drops when clouds form, explaining the upper cut-off in the NOMAD profiles as HDO becomes undetectable
- NOMAD water ice observations provide evidence that fractionation by clouds is the main factor controlling the HDO distribution on Mars

Correspondence to:
F. Daerden,
Frank.Daerden@aeronomie.be

Citation:
Daerden, F., Neary, L., Villanueva, G., Liuzzi, G., Aoki, S., Clancy, R. T., et al. (2022). Explaining NOMAD D/H observations by cloud-induced fractionation of water vapor on Mars. *Journal of Geophysical Research: Planets*, *127*, e2021JE007079. https://doi.org/10.1029/2021JE007079

Received 1 OCT 2021
Accepted 15 JAN 2022

Author Contributions:
Conceptualization: F. Daerden
Data curation: F. Daerden, L. Neary, G. Villanueva, G. Liuzzi, I. R. Thomas, B. Ristic
Formal analysis: F. Daerden
Funding acquisition: A. C. Vandaele
Investigation: F. Daerden, L. Neary, G. Villanueva, G. Liuzzi, J. A. Whiteway
Methodology: F. Daerden, L. Neary
Project Administration: A. C. Vandaele
Resources: F. Daerden, L. Neary, G. Villanueva, G. Liuzzi, S. Aoki, M. D.

Abstract

The vertical profiles of water vapor and its semi-heavy hydrogen isotope HDO provided by instruments on ExoMars Trace Gas Orbiter constitute a unique new data set to understand the Martian water cycle including its isotopic composition. As water vapor undergoes hydrogen isotopic fractionation upon deposition (but not sublimation), the D/H isotopic ratio in water is a tracer of phase transitions, and a key quantity to understand the long-term history of water on Mars. Here, we present 3D global simulations of D/H in water vapor and compare them to the vertically resolved observations of D/H and water ice clouds taken by NOMAD during the second half of Mars year 34. D/H is predicted to be constant with height up to the main cloud level, above which it drops because of strong fractionation, explaining the upper cut-off in the NOMAD observations when HDO drops below detectability. During the global and regional dust storms of 2018/2019, we find that HDO ascends with H_2O, and that the D/H ratio is constant and detectable up to larger heights. The simulations are within the provided observational uncertainties over wide ranges in season, latitude and height. Our work provides evidence that the variability of the D/H ratio in the lower and middle atmosphere of Mars is controlled by fractionation on water ice clouds, and thus modulated by diurnally and seasonally varying cloud formation. We find no evidence of other processes or reservoirs that would have a significant impact on the D/H ratio in water vapor.

Plain Language Summary

The isotopic composition of atmospheric water on Mars provides insights about the phase transitions in the water cycle, because the light (H_2O) and semi-heavy (HDO) form of water vapor deposit at different saturation pressures. Knowing the isotopic composition of atmospheric water also provides insights on the long-term evolution of water on Mars. The NOMAD instrument on ExoMars Trace Gas Orbiter provided the first vertical profiles of the D/H ratio in water vapor on Mars. The data set shows a large variability with season and latitude. To understand this behavior, a general circulation model is required. We provide detailed simulations of the D/H ratio in Martian water vapor and compare them with the NOMAD observations. The model predicts that the D/H ratio is constant in the lower atmosphere and decreases across a layer of strong cloud formation that varies with season. During the global dust storm of 2018, this cloud layer was severely lifted. The simulations compare well to the observations, both out and in the dust storm, and explain their upper cut-off by this predicted decrease in D/H. No other processes than cloud formation, nor special surface ice reservoirs with strongly different D/H values, were needed to reproduce the observations.

1. Introduction

A strong marker for the evolution of water in the atmosphere of Earth is the ratio between water and its most common isotope: semi-heavy water (HDO; e.g., Dansgaard, 1964; Hoffmann et al., 2000; Jouzel, 1986; Jouzel et al., 1997; Randel et al., 2012). (The heavy water isotope, D_2O, is several orders of magnitude less abundant.) Also on Mars, it is expected that the HDO/H_2O isotopic ratio is an important marker for atmospheric water vapor

Smith, M. J. Wolff, A. Pankine, A. Khayat, B. Cantor, J. Erwin, C. Depiesse, A. Piccialli, S. Robert, L. Trompet, Y. Willame, E. Neefs, I. R. Thomas, B. Ristic, A. C. Vandaele
Software: F. Daerden, L. Neary
Supervision: F. Daerden
Validation: F. Daerden
Visualization: F. Daerden
Writing – original draft: F. Daerden
Writing – review & editing: F. Daerden, L. Neary, G. Villanueva, G. Liuzzi, S. Aoki, R. T. Clancy, J. A. Whiteway, B. J. Sandor, A. Pankine, A. Khayat, R. Novak, M. Crismani, M. J. Mumma, S. Viscardy, A. Mahieux, A. C. Vandaele

(e.g., Bertaux & Montmessin, 2001; Fouchet & Lellouch, 2000; Montmessin et al., 2005). HDO is known to have a slightly smaller saturation pressure than H_2O, and so will deposit more rapidly with decreasing temperature. This results in a relative enhancement of HDO in the ice phase, a process called isotopic fractionation, and diagnosed with the numeric ratio of HDO/H_2O volume mixing ratios (VMRs; for simplicity abbreviated as D/H, which is strictly speaking the ratio of D to H atoms in water, and differs from the former by a factor two). This ratio is expressed in terms of the Vienna Standard Mean Ocean Water (VSMOW) on Earth, for our definition of D/H in water set at $2 \times 155.76 \times 10^{-6}$. Also, photolysis can lead to hydrogen fractionation in water (Yung et al., 1988). And in the upper atmosphere, D and H atoms have different atmospheric escape rates (Krasnopolsky et al., 1998). Therefore, it is expected that hydrogen fractionation in water vapor contains the key to understand the long-term history of water on Mars (Alsaeed & Jakosky, 2019; Jakosky, 2021).

This paper focuses on fractionation by cloud formation and direct surface deposition, and on present-day, short time-scale (i.e., diurnal to seasonal) processes in the hydrological cycle on Mars. When an air parcel travels through the atmosphere, driven by physical processes such as advection, turbulence and diffusion, and encounters conditions for water ice cloud formation, the water vapor will undergo hydrogen (and oxygen) isotopic fractionation, and its D/H ratio will change along the trajectory. On the larger spatial and temporal scales, this will result in a specific, varying distribution of the D/H ratio in the atmosphere, that will depend on diurnal and seasonal atmospheric forcing (Montmessin et al., 2005).

Until recently, the D/H ratio in the atmosphere of Mars was only known from occasional observations by Earth-based telescopes (Aoki et al., 2015; Encrenaz et al., 1991, 2001, 2016, 2018; Khayat et al., 2019; Krasnopolsky, 2015; Krasnopolsky et al., 1997; Novak et al., 2011; Owen et al., 1988; Villanueva et al., 2015). These observations provided the ratio of the total water and HDO column abundances (typically of the order of 5.5–8 × VSMOW). One in situ determination of D/H = 5.95 × VSMOW at the surface was provided by Webster et al. (2013). In addition, an upper atmospheric D/H value, in H_2, of 2.2 was obtained by Krasnopolsky and Feldman (2001). The arrival of the MAVEN (Clarke et al., 2017; Mayyasi et al., 2019) and ExoMars Trace Gas Orbiter (TGO) missions began a paradigm shift in our knowledge of D/H in the Martian atmosphere. While MAVEN focused on the upper atmosphere, two instruments on TGO, NOMAD (Vandaele et al., 2018, 2019), and ACS (Korablev et al., 2018, 2019), took the first vertically resolved measurements of D/H in the lower and middle atmosphere (Vandaele et al., 2018). The D/H ratio was derived from simultaneous detections of HDO and H_2O spectral lines during highly sensitive solar occultation observations. Recently, Villanueva et al. (2021) presented the first extensive climatology for D/H on Mars from NOMAD observations, consisting of almost 2,000 profiles taken during the first half Martian year of NOMAD science operations (April 2018–April 2019, corresponding to the second half of Mars year [MY] 34). This data set showed an intriguing variability over latitude, altitude and time. The D/H value in the lower atmosphere was estimated at 6–7 × VSMOW, consistent with previous observations, but it was found to decrease to 2–3 × VSMOW in the middle atmosphere.

For a profound understanding of this data set, global atmospheric modeling is required to precisely integrate all the physical processes at play (transport, mixing, and cloud formation) while they vary with latitude, geography, altitude and with time of year. Here, we use the three-dimensional general circulation model (GCM) Global Environmental Multiscale model for Mars (GEM-Mars), that includes a complete water cycle (Daerden et al., 2019; Neary & Daerden, 2018), to simulate the fractionation of water upon deposition and to follow its seasonal trends. The simulation results will be compared in detail to the vertical profiles of D/H obtained from NOMAD (Villanueva et al., 2021).

NOMAD and ACS witnessed a Global Dust Storm (GDS) in 2018 during the first year of TGO observations. It was found that this storm caused a strong redistribution of water vapor (Aoki et al., 2019; Fedorova et al., 2020; Neary et al., 2020; Vandaele et al., 2018). To assess the impact on the D/H ratio during this event, we will also include a simulation of this GDS, based on the work of Neary et al. (2020) which could reproduce the observed impact of the storm on the distribution of water vapor.

This study follows up on the pioneering work of Montmessin et al. (2005) who presented the first global simulations of HDO on Mars. Since then, models have progressed, for instance regarding the radiative impact of water ice clouds (Haberle et al., 2019; Navarro et al., 2014; Neary & Daerden, 2018) and the enrichment of species upon CO_2 deposition (e.g., Lian et al., 2012; Smith et al., 2018; Sprague et al., 2007, 2004). Recently, Rossi et al. (2021) applied the model of Montmessin et al. (2005) for the conditions of the 2018 GDS, but without

including these processes. Our model includes a simple cloud formation scheme but with full radiative cloud feedbacks and with noncondensable gas enrichment. The combination of a new HDO simulation with the first highly vertically resolved data set of water vapor and D/H, allows to make a unique assessment of the variation of D/H with seasons, latitude and height on the global scale, and both inside and outside of dust storm conditions, and so to provide a next step forward in understanding water on Mars.

This paper is organized as follows. After introducing the model and in particular the HDO simulation in Section 2, we will provide a detailed overview of the simulation results on various spatial and temporal scales (columns, profiles, and on diurnal and seasonal scales) in Section 3. Section 4 presents the D/H simulation in GDS conditions. Section 5 provides a detailed comparison to the NOMAD D/H vertical profile data set. We end with conclusions.

2. Simulating the D/H Cycle on Mars

2.1. The GEM-Mars GCM

To simulate the hydrological cycle on Mars, we apply the GEM-Mars model. GEM-Mars is a 3D grid-point based general circulation model for the atmosphere of Mars. It is described and evaluated in Daerden et al. (2015), Neary and Daerden (2018), Smith et al. (2018), Daerden et al. (2019), Neary et al. (2020), Bouche et al. (2021) and Newman et al. (2021). The model is operated on a horizontal resolution of $4° \times 4°$ (45 by 90 grid points) and on 103 hybrid vertical levels ranging from the surface to about 150 km altitude, with a time step of 30.8246 min (1/48th of a Mars solar day or sol). GEM-Mars contains routines for radiative transfer through an atmosphere containing CO_2 gas, dust and water ice clouds, and also for subsurface heat transfer (including shallow subsurface ice at high latitudes), for turbulent convection in the Planetary Boundary Layer (PBL), for molecular diffusion, and for gravity wave drag. The model has a CO_2 deposition/sublimation cycle and an interactive surface pressure correction. The vertical distribution of dust can be either self-consistently calculated from dust that is lifted from the surface by shear wind stress and dust devils (Daerden et al., 2015, 2019; Musiolik et al., 2018; Neary & Daerden, 2018), or prescribed using a predefined vertical profile shape (Neary et al., 2020). In both cases, dust total optical depths and their spatiotemporal variation can also be chosen to be constrained by a dust optical depth climatology, such as those provided by Montabone et al. (2015, 2020).

The model includes a water cycle including northern and southern permanent caps, clouds and transient surface ice deposits. Recently, the formation of clouds was improved in the model compared to previous model versions. In particular, in previous model versions clouds were prevented from forming in the north polar summer season to avoid excessive radiative feedbacks. Here, by imposing large ice particle radii over the north polar summer cap, the particles sediment much faster than before, and much less optically thick clouds will form, solving the excessive feedback problem. This kind of solution for models with simple cloud schemes was already mentioned in Haberle et al. (2019). We apply an ice particle radius of 150 µm over the permanent cap in summer (L_s = 80°–150°). This is close to particle sizes that were simulated for the sub-polar Phoenix site (Daerden et al., 2010). The importance of north polar summer clouds for the D/H cycle was explained in Montmessin et al. (2005). As the permanent water ice cap in summer is the only source of HDO in the model, such clouds will act as a filter to reduce the D/H ratio from that in the cap to lower values as water ascends into the atmosphere and is fractionated on these clouds. If the presence of these clouds is too strong, they will reduce the D/H value too much. Only a reasonable simulation of north polar summer clouds will allow the model to estimate the good relationship between D/H in the ice cap and in the atmosphere.

For the present study, the model is initialized with a water ice reservoir of 10^6 pr-µm (an arbitrary but large amount) in the permanent north polar cap, and no water anywhere else. The permanent cap is defined as consisting of the grid cells north of 80° latitude for which the surface albedo (taken from the Thermal Emission Spectrometer (TES, Christensen et al., 2001) and averaged over the model grid cells) is larger than 0.23, complemented with the grid cells between 70° and 80°N latitude and for longitudes between 90° and 270°E where the surface albedo is larger than 0.24. The cap's area is shown in Figure 1. It is nearly identical to the permanent cap defined in the NASA/Ames Legacy model (Haberle et al., 2019). The albedo of the exposed cap can be set as a parameter in the model (here set to 0.33), and this value is modified to a higher value (0.6) at sites covered with CO_2 ice. The thermal inertia of the cap can also be set as a parameter (here set to 700 $J/m^2/K/s^{1/2}$). Water sublimates from the grid cells in the cap if they are not covered by CO_2 surface ice and if the water partial vapor

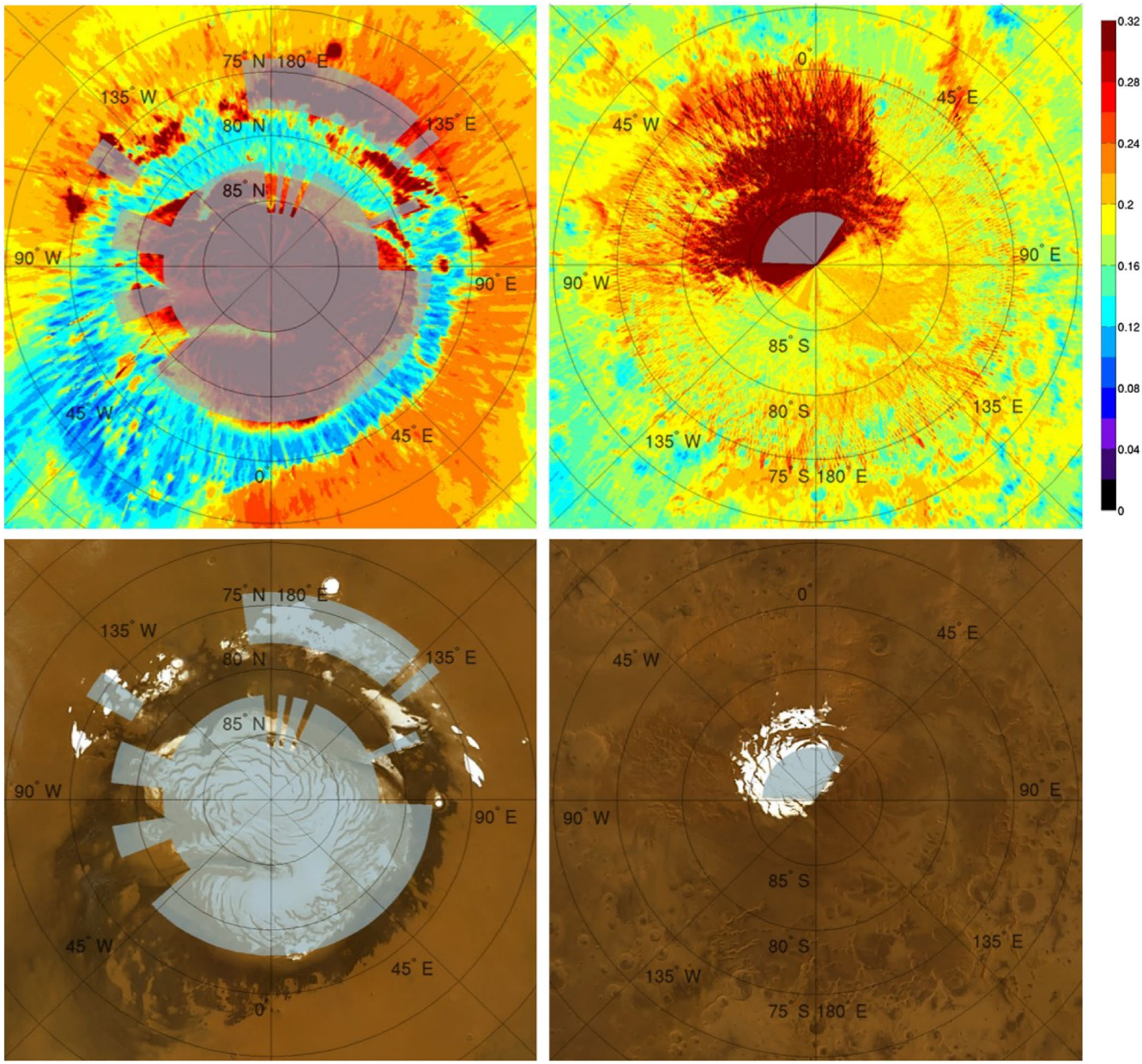

Figure 1. Definition of the permanent polar ice caps in the model (gray shaded areas). Left: north polar permanent water ice cap. Right: south polar permanent CO_2 ice cap. The background in the top plots is the Thermal Emission Spectrometer albedo (Christensen et al., 2001), in the bottom plots the background are dust and cloud-free MARCI color stereographic mosaics (north pole: 26 January 2018, $L_s = 120°$ and south pole: 28 December 2018, $L_s = 314°$), provided by B. Cantor (MSSS). These allow to compare the caps defined in the model to the visible presence of surface ice.

pressure is below the saturation pressure following Marti and Mauersberger (1993) for temperatures above 169 K and Mauersberger and Krankowsky (2003) for lower temperatures.

Atmospheric water is transported by PBL turbulent mixing and by advection, and deposits into ice clouds if the partial pressure exceeds the saturation pressure (100% RH). Ice water content (IWC) is stored as VMR in a single tracer that is transported like the other tracers, but is also sedimenting. Water ice particle radii are prescribed in the model, and set to 1 μm above 10 km, 2 μm between 5 and 10 km, and 8 μm below 10 km. This was done to reflect the fact that water ice particles are likely larger in the lowest scale height (e.g., Whiteway et al., 2009, and Daerden et al., 2010). As mentioned above, in the northern summer season, the ice particle radii are set to 150 μm below 10 km over the permanent cap. This is sufficient to overcome the formation of optically thick clouds as

these particles sediment fast (2.46 m/s). In all cases a fixed amount of 80% of the IWC is sedimented. In the lowest model layer (of ~12.5 m thickness), additional water vapor can also deposit directly onto the surface if the water vapor partial pressure exceeds the saturation pressure when calculated using the surface temperature. Transient surface water ice is stored in a separate field from the one that contains ice in the permanent ice cap, to make a physical distinction between ice condensing from the present-day atmosphere, and the perennial ice which is assumed to be more ancient (e.g., Alsaeed & Jakosky, 2019; Fisher, 2007; Jakosky, 2021; Villanueva et al., 2015). The water ice tracer can sublimate if the water vapor partial pressure in the same grid cell becomes lower than the saturation pressure. On the permanent water ice cap, transient ice is sublimated first before any permanent ice is sublimated. The model also includes a residual south polar cap, which is defined as the grid cells south of 86°, between longitudes 270° and 30°E (passing clockwise through 0°E), as shown in Figure 1. The surface temperature at this residual cap is always kept to the CO_2 frost temperature. It is therefore a pure sink for water vapor.

2.2. Simulating D/H Isotopic Fractionation Upon Vapor Deposition

HDO, the semi-heavy isotope of water, is implemented in the model in a way similar to normal water. The permanent north polar cap is initialized with an amount of HDO that can be chosen at the start of the simulation. As we will show, the amount leading to the best comparisons with NOMAD data is 6 × VSMOW. In the model, HDO can only deposit when H_2O deposits, and is enriched in the ice phase by a factor of α_{HDO}, which is given by Lamb et al. (2017) and is valid for temperatures at least down to 189 K (but is assumed here to be still valid for lower temperatures):

$$\alpha_{HDO} = \exp\left(13,959/T^2 - 6.19 \times 10^{-2}\right)$$

For the range of temperatures found in the lower Martian atmosphere, the factor α_{HDO} varies between 1.13 at 273 K and 1.75 at 150 K.

Montmessin et al. (2005) explored two different scenarios for the implementation of HDO deposition in a model. A first one was Rayleigh distillation (Dansgaard, 1964; Rayleigh, 1902), which assumes that fractionation occurs slowly, with immediate removal of the condensate from the vapor after formation, and that only the instantaneous flux of deposition is at isotopic equilibrium with the gaseous phase. This is often applied as a first approach to model water vapor fractionation by clouds or snow on Earth (Gedzelman & Arnold, 1994; Jouzel, 1986; Jouzel & Merlivat, 1984; Jouzel et al., 1997). The other scenario considered rapid isotopic homogenization. This is more applicable for liquid particles, but Montmessin et al. (2005) argued that the timescale for isotopic diffusion in ice particles intersects with typical timescales for deposition and sedimentation on Mars, and could therefore not rule out that such a process also takes place on Mars. Their final results indicated that in most cases, there were no large difference between the two approaches.

In this paper, we will only consider the pure Rayleigh distillation process. (We will discuss this assumption in Section 5.6.) This means that if an amount ΔH_2O (expressed in VMR) is depositing into the ice phase (in clouds or onto the surface), an amount ΔHDO of HDO will sublimate with it:

$$\Delta HDO = \alpha_{HDO} \times \Delta H_2O \times x_{HDO}/x_{H2O}$$

In this expression, x_{HDO} and x_{H2O} represent the volume mixing ratios of both species before deposition. Given the model time step of 30′, occasionally ΔH_2O becomes comparable to x_{H2O}, typically near the edges of the seasonal polar caps, and only in the lowest, near-surface model levels. In those cases, there may be less HDO available for deposition than the fractionation factor would allow for. However, in those cases the involved mixing ratios are usually very low and we expect the impact to be small.

Likewise, HDO can only sublimate when H_2O sublimates, however, no fractionation is assumed to take place in this process because of the slow molecular diffusion of isotopes within ice (e.g., Fouchet & Lellouch, 2000; Montmessin et al., 2005). In this case, if an amount ΔH_2O (expressed in VMR) is sublimating from the ice phase, an amount ΔHDO of HDO will sublimate with it:

$$\Delta HDO = \Delta H_2O \times x_{HDO}/x_{H2O}$$

In this expression, in the case of sublimation from ice clouds, x_{HDO} and x_{H2O} represent the volume mixing ratios of both species in the ice phase before sublimation. However, if the sublimation occurs from surface ice, x_{HDO} and x_{H2O} represent the water ice columns (expressed in particles/m^2) of both species on the surface (in the transient surface water ice field) before sublimation. For grid cells on the permanent north polar cap that are not covered by CO_2 surface ice, and which are no longer covered by transient water ice, x_{HDO} and x_{H2O} represent the water ice columns of both species in the permanent cap (the ratio of which is always fixed and defined by the initial setting). It was also found that the D/H ratio can reach spurious values in the polar regions during winter where the water vapor abundance becomes low. This is a numerical artifact of the advection process and a similar problem was recently discussed in Rossi et al. (2021). Their solution existed in advecting rather the D/H ratio than the VMR of HDO. The current tracer scheme in GEM-Mars does not yet allow for a similar treatment. However, this numerical problem is only weakly present in GEM-Mars, and to remove most of the spurious values it turns out to be sufficient to apply the solution of Rossi et al. (2021) only for the locations with low water vapor abundance (below 0.5 ppmv), for which the impact on the tracer scheme is negligible.

This implementation of HDO is rather basic, assuming simple mass balances, and it does not yet consider any microphysical processes. The results presented in this paper should therefore be considered as first estimates based on the simple cloud and surface ice formation scheme of the current GEM model.

3. Simulations and Results

3.1. Dust Scenarios and Model Set-Up

As we want to compare the simulations to the observations from NOMAD taken during the second half of MY 34 (April 2018–January 2019), we have to pay special attention to the dust scenarios that are used. In this period a large GDS occurred. To simulate the conditions in MY34, the total dust optical depth climatology of Montabone et al. (2020) is applied, as was already done in our previous model study of the GDS (Neary et al., 2020). To evaluate the impact of the GDS on the simulations, we will also simulate a typical MY (i.e., with no GDS) as a reference. For this we choose the dust climatology for MY33 (Montabone et al., 2015, 2020) which had no large dust storm, the dust climatology was available at the start of this work, and it looks similar to many years without a GDS (see Montabone et al., 2015).

The vertical dust profile is self-consistently calculated in the model, with dust being lifted from the surface by wind shear and dust devils, and being transported by the calculated mixing, advection, and sedimentation. The so obtained dust profiles are then scaled uniformly to match the total optical depths of the climatologies. However, during the GDS, the model dust will not ascend high enough in the atmosphere as demonstrated by Neary et al. (2020), and the vertical dust distribution during the GDS could only be approximated when imposed using a Conrath distribution (Conrath, 1975; Forget et al., 1999) for the dust mass mixing ratio (MMR):

$$q(z) = q_0 \times \exp\left(\nu \times \left(1 - \frac{p_0}{p}\right)^{\frac{70}{z_{max}}}\right)$$

with p the pressure, subscript "0" referring to surface values, and z_{max} is L_s- and latitude-dependent as defined in Montmessin et al. (2004).

We refined the simulation of Neary et al. (2020) in two aspects. First, the Conrath dust distribution is only applied in a time window around the GDS: L_s = 160°–230°. Later, in the same Martian year, a regional dust storm (RDS) occurred during which also a large redistribution of water vapor was observed (Aoki et al., 2019; Chaffin et al., 2021). We found that also during the RDS the normal model dust would not lead to the level of redistribution that was observed, and we will also apply the Conrath profile from L_s = 315°–330° for the RDS.

The second refinement considers the Conrath shape parameter ν, which was fixed in Neary et al. (2020). This parameter describes the decrease of the dust profile with altitude, and the higher it is the faster the dust profile will decrease. We assume that the dust profile will only increase to high altitudes during periods and at locations of high dust optical depths. To simulate this, we developed a simple parameterization for the parameter ν, in which ν is simply varying linearly as a function of the total dust optical depth between the two extreme values that were used in Neary et al. (2020): 8×10^{-4} and 7×10^{-3}:

$$\nu = \max\left(8\times10^{-4},\left(\min\left(\ 7\times10^{-3},\ \ a\times\tau+b\right)\right)\right)$$

with τ the visible dust optical depth at the location. The coefficients a and b are set based on some first comparisons with dust extinction profiles from the Mars Climate Sounder (Kleinböhl et al., 2009, 2011): $a = -2.21\times10^{-3}$ and $b = 7.44\times10^{-3}$.

The model is first run for a long time with the MY33 dust climatology that is annually repeated. It takes several Martian years for the water and HDO cycles to build up from scratch and stabilize, with annually repeating seasonal surface water deposits on the polar caps, and annually repeating cloud formations such as the aphelion cloud belt (ACB). The permanent water ice cap in the north acts as a pure source and is eroded repeatedly every year during northern summer (between roughly L_s ~90° and 120°). The released water is increasing the total atmospheric water content, which also causes an increase of water in the transient cloud and surface ice reservoirs. The only pure sink of water vapor and HDO in the system is the residual south polar cap, which is much smaller in area than the permanent north polar cap (in the model: 5.79×10^4 km^2 vs. 1.29×10^6 km^2, or ~4.5%). The total atmospheric budget of water is reaching a steady state with small (~1%) interannual variations after ~10 Martian years.

We here present results of simulations of one MY that start with the final state of the long spin-up simulation. For the *standard* simulation, this is again MY33, while for the *GDS* simulation this is the MY34 dust climatology. In the subsections below, we will focus on D/H in water and present a variety of results, on different spatial and temporal scales: total columns, vertical profiles, seasonal evolution, diurnal, and spatial variability.

3.2. D/H Simulation: Total Columns, Seasonal Evolution

The seasonal distribution of total column HDO (not shown) follows a similar pattern as that of H_2O (shown as contours in Figure 2, top). As a result, except for the polar regions during winter, the simulated "D/H" ratio of total HDO and H_2O columns shows no strong variation with the time of year or latitude (Figure 2). The bulk atmospheric value of D/H shows only small seasonal variations. (The variations that are visible will be discussed later in this section.) Between 40° north and south, the annual mean value is 5.7 × VSMOW. This represents a decrease to the ratio originally defined in the north polar permanent cap (6 × VSMOW) of 5%. This loss actually occurred in the first year of the spin-up simulation, when the first water vapor was released in a dry atmosphere and the first clouds and transient surface ice deposits formed. After that, the annual D/H budgets remain well balanced with no additional loss. This indicates the importance of the initialization of the model simulations for drawing any strong conclusions on the relationship between the D/H in the perennial ice and in the atmosphere. (We will discuss this further down.)

As is expected from the implementation, the D/H in water ice clouds and surface ice deposits is higher than in vapor. As mentioned before, we consider transient ice separate from permanent ice, and sublimate transient ice before any permanent ice. The D/H in transient ice reflects that of the atmosphere, as it is composed of atmospheric deposits. This constitutes a feedback that keeps the atmospheric D/H low. In addition, we find that also the permanent ice is eroded every year, meaning that the final atmospheric D/H is composed of a mixture of that of the permanent and transient ices, which will always be lower than that of pure perennial ice. At the residual cap in the south, HDO and H_2O are permanently removed from the atmosphere. All these processes are well in balance in our simulation and keep the D/H cycle very stable throughout the years.

To better understand the D/H exchanges near the surface, especially in the polar regions, Figure 3 shows the D/H values at the surface in the different components (gas, clouds, transient surface ice, and permanent surface ice) for selected latitudes. In the north polar hood, the gas-phase D/H increases to 5.6 × VSMOW during summer. D/H in transient surface ice increases at that time to 7 × VSMOW. During winter, when most of the HDO has deposited onto the surface, D/H in the transient ice on the seasonal polar cap decreases. At 88°N (not shown) the D/H in transient ice approaches 6 × VSMOW, that is, the value of the permanent ice cap, but at 80°N it decreases to 5.6 × VSMOW, so lower than the value of permanent ice, as a result of the feedback mechanism just described.

Figure 3 shows another interesting feature: the D/H in the southern seasonal cap becomes higher (up to 6 × VSMOW, so the same as in the permanent cap) than that in the northern seasonal cap. This is a result of the surface temperatures being lower in the south during winter, depositing relatively more HDO than in the north.

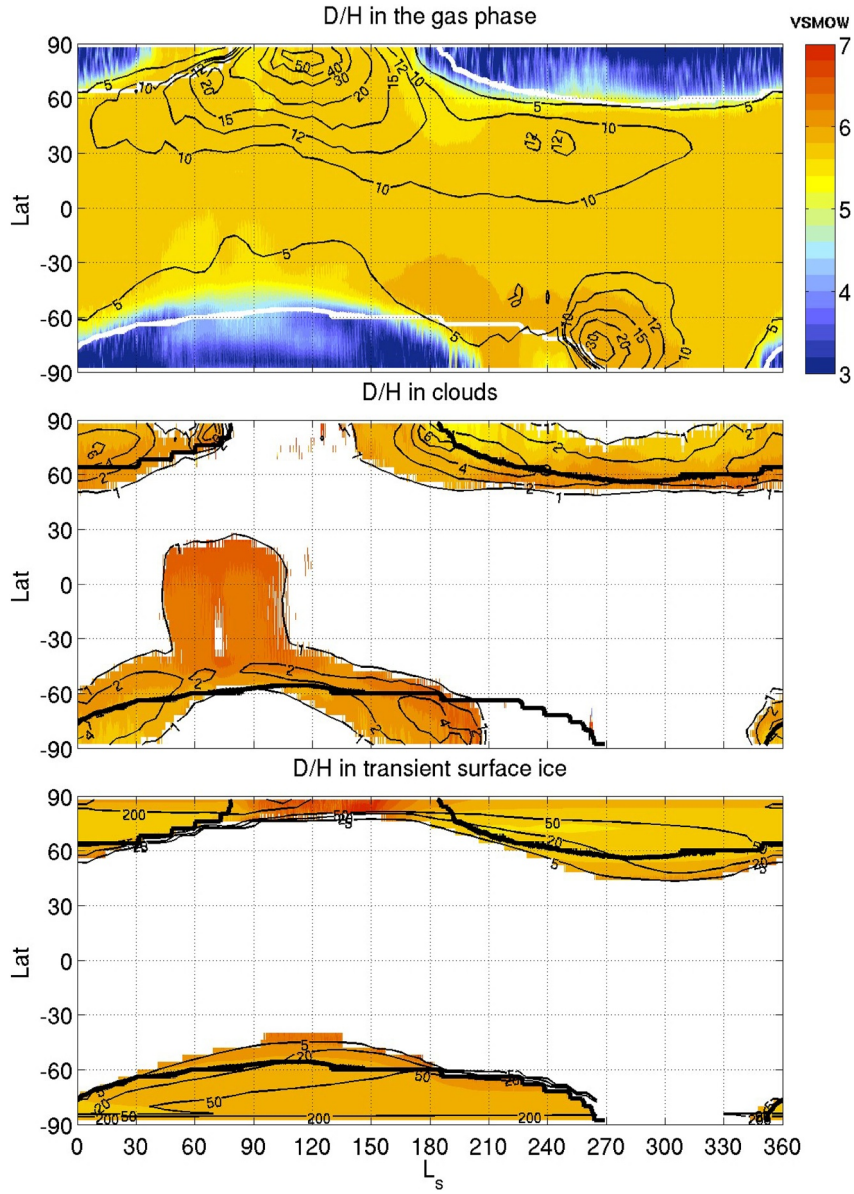

Figure 2. Overview of D/H simulation results, for the gas-phase (top), clouds (middle) and surface ice (bottom). Color shading represents D/H ratio of HDO and H_2O (gas or ice) total columns expressed in Vienna Standard Mean Ocean Water and zonally averaged over all longitudes and local times, at the model's time resolution (30′). Thin black contours represent water column (top), cloud water ice column (middle) and surface ice (bottom), in pr-μm. For clouds and surface ice only values are shown when the total ice column exceeds 1 pr-μm. D/H in surface ice shows the value in transient surface ice. The thick (white, black) contour lines show the calculated edges of the seasonal CO_2 polar caps (zonal mean CO_2 mass exceeding 10^{10} kg).

As a result, southern summer gas-phase D/H values are also predicted to be higher (6 × VSMOW) than in northern summer. This can also be seen in Figure 2 (top), as D/H is larger in the southern hemisphere after sublimation of the southern seasonal cap, compared to the other parts of the planet throughout the year. Unlike in the north, there are no water ice clouds in summer in the south and the D/H of the seasonal cap is readily transferred to that of the atmosphere without additional filtering.

Around aphelion at southern latitudes, the D/H values are somewhat below the average. The ACB removes a considerable amount of HDO from the gas-phase (as will be shown in Section 3.3) but it is located at heights (30–40 km, see Section 3.3) large enough not to appear in the total column D/H. There is rather some low-level

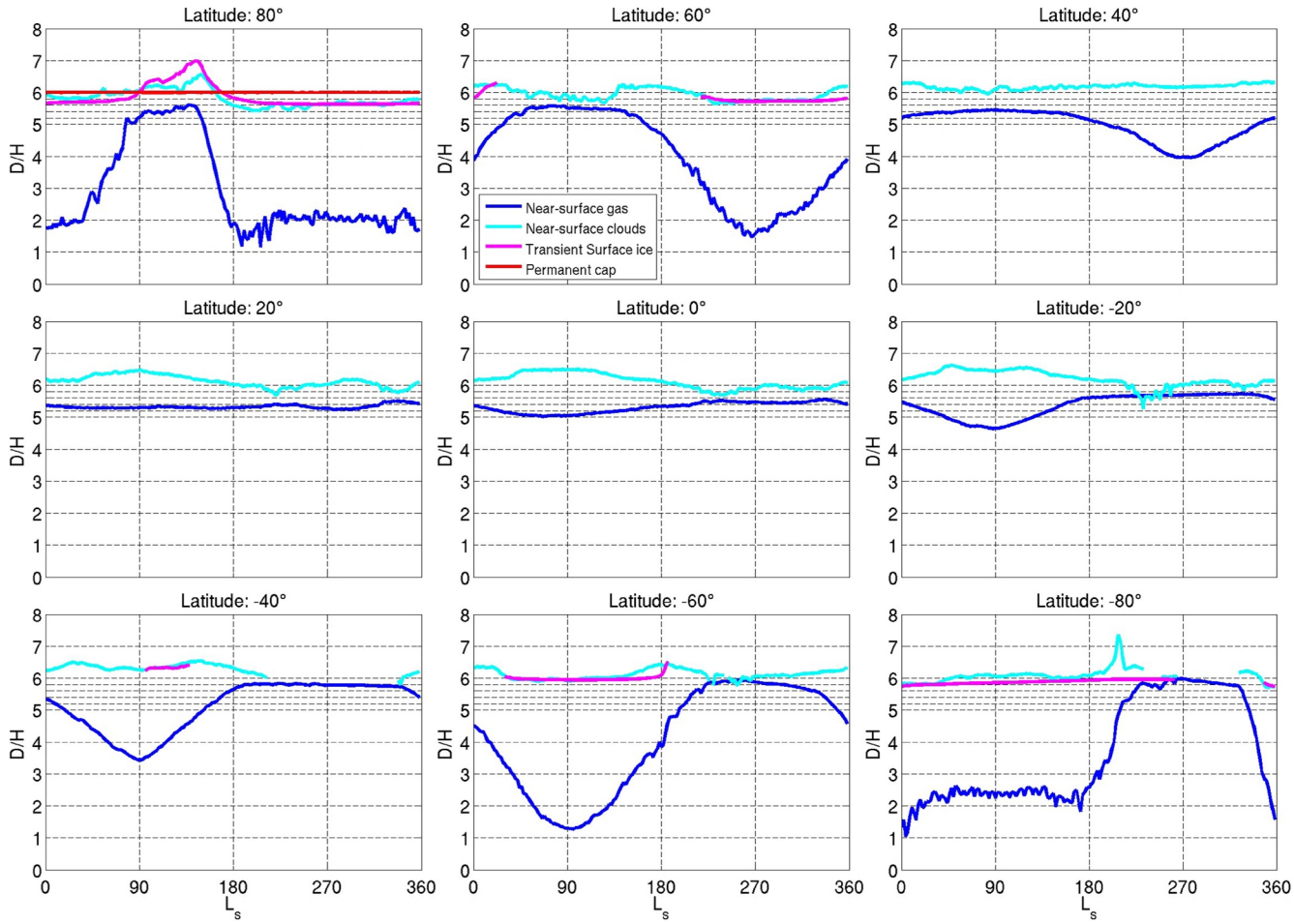

Figure 3. D/H exchanges at the surface. The figure shows the time evolution of the zonally averaged D/H ratio at the surface in the model for selected latitudes. The D/H ratio was zonally averaged over all longitudes and local times and binned over 2° L_s. Between 5 and 6 × Vienna Standard Mean Ocean Water (VSMOW), the grid lines are spaced 0.2 × VSMOW.

ice cloud formation at this time that contributes to the small decrease of D/H column. Comparison of the simulated clouds with those reported in Smith (2004), Olsen et al. (2019), and Giuranna et al. (2021) indicates that these clouds are not actually occurring at this time and place. This was conjectured already in Daerden et al. (2019) from comparisons with MARCI ozone column observations.

3.3. Vertical Profiles, Seasonal Evolution

Figure 4 shows the simulated vertical distribution of water vapor and D/H at the four cardinal seasons of the Martian year. The distributions of H_2O and D/H are similar, but D/H drops more strongly with height because of fractionation by water ice clouds in a zone of strong cloud formation in the lower and middle atmosphere, the so-called *hygropause* region (Figure 5). These clouds constitute a barrier for further upwards transport of water vapor. Clouds at those altitudes will not sediment to the surface, but the diurnal cycle of cloud formation and sedimentation, followed by sublimation, acts to confine the bulk of the water vapor distribution to below this height. This causes a strong drop in the water vapor abundances with height, hence the name hygropause. The role of the hygropause for HDO was first predicted by Bertaux and Montmessin (2001), coining also the name *deuteropause*. As HDO is enhanced in water ice clouds compared to normal water, the effect of cloud formation will be stronger for HDO, and this explains why the D/H ratio drops more strongly than H_2O.

The D/H value is more or less constant in the lower atmosphere at low latitudes, and decreases with height across the cloud zone. In the lower atmosphere the D/H value is the same as that of the total water and HDO columns that

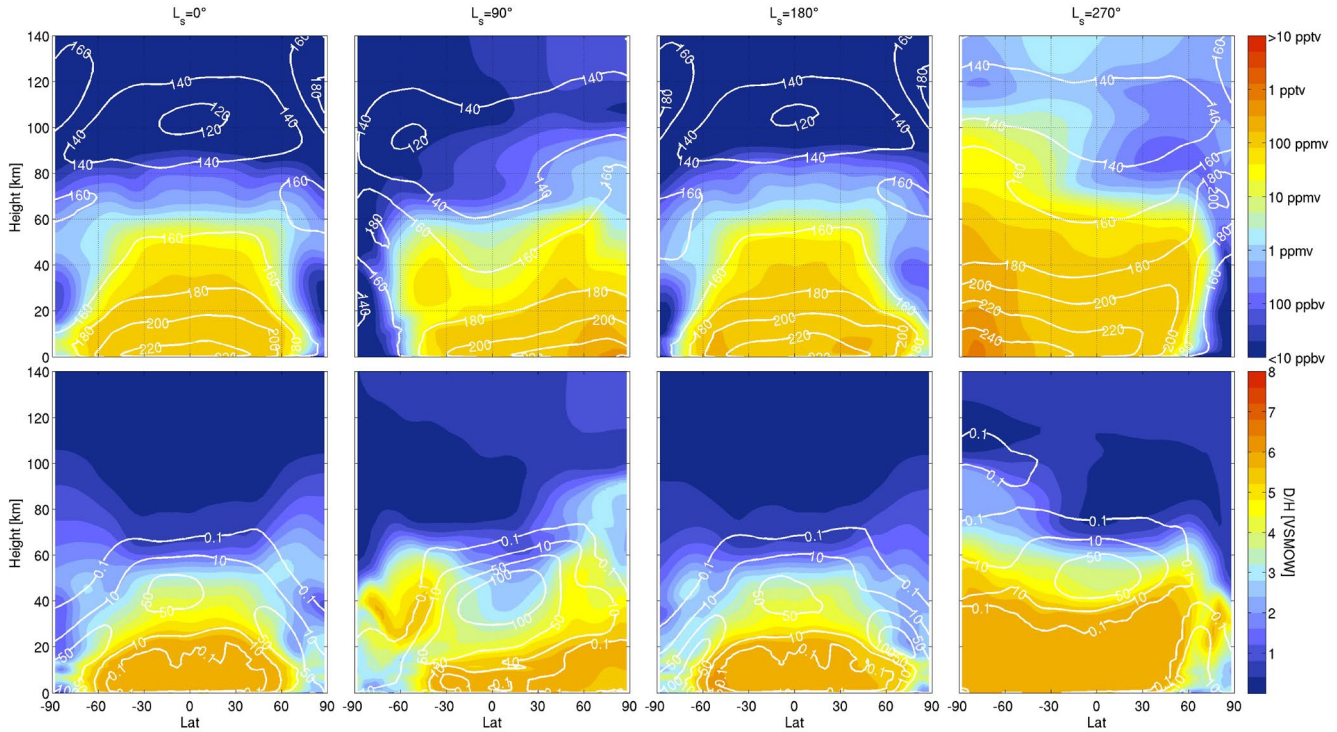

Figure 4. Latitude-height zonal mean vertical distribution of water vapor (top) and D/H in the gas-phase (bottom) for the four cardinal seasons, averaged over all longitudes and local times and over 10 sols. Contours represent the temperature (in K, top) and ice water content (in ppmv, bottom) as indication where clouds form.

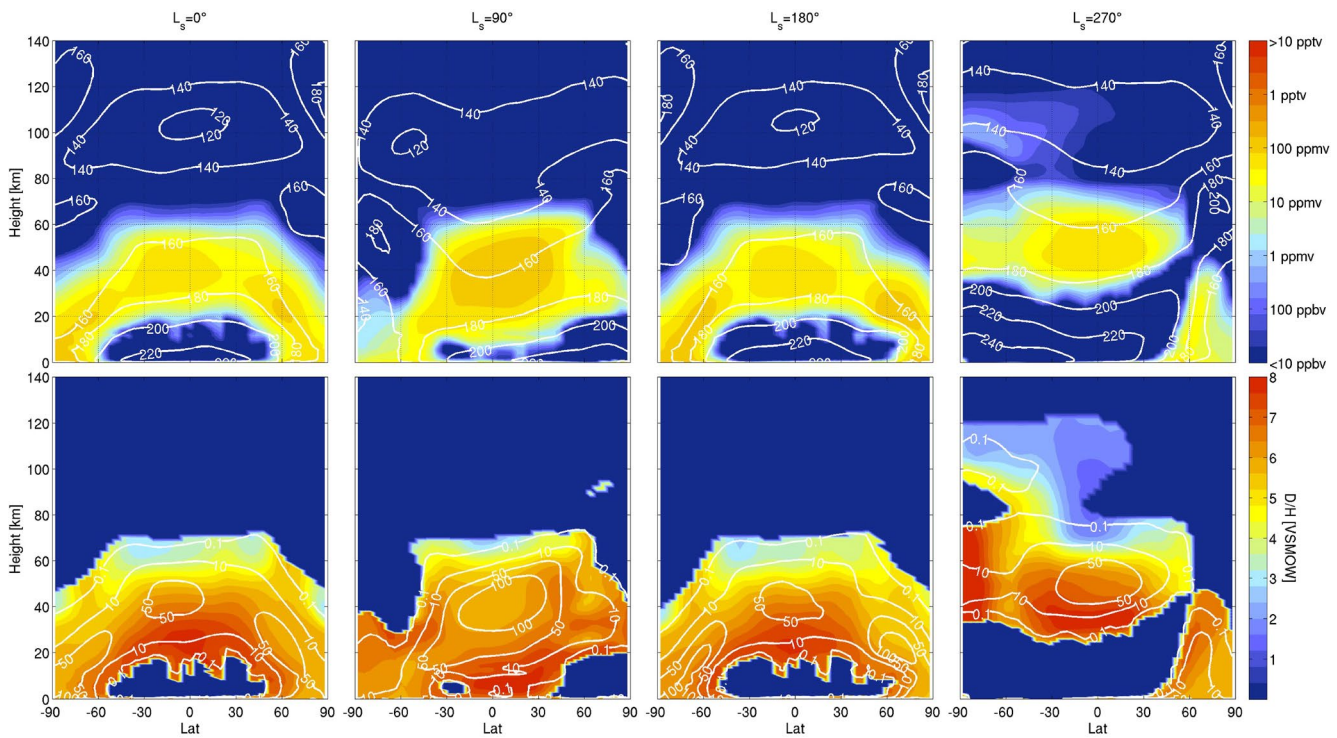

Figure 5. Same as Figure 4, but showing ice water content (top) and D/H in the ice phase (bottom).

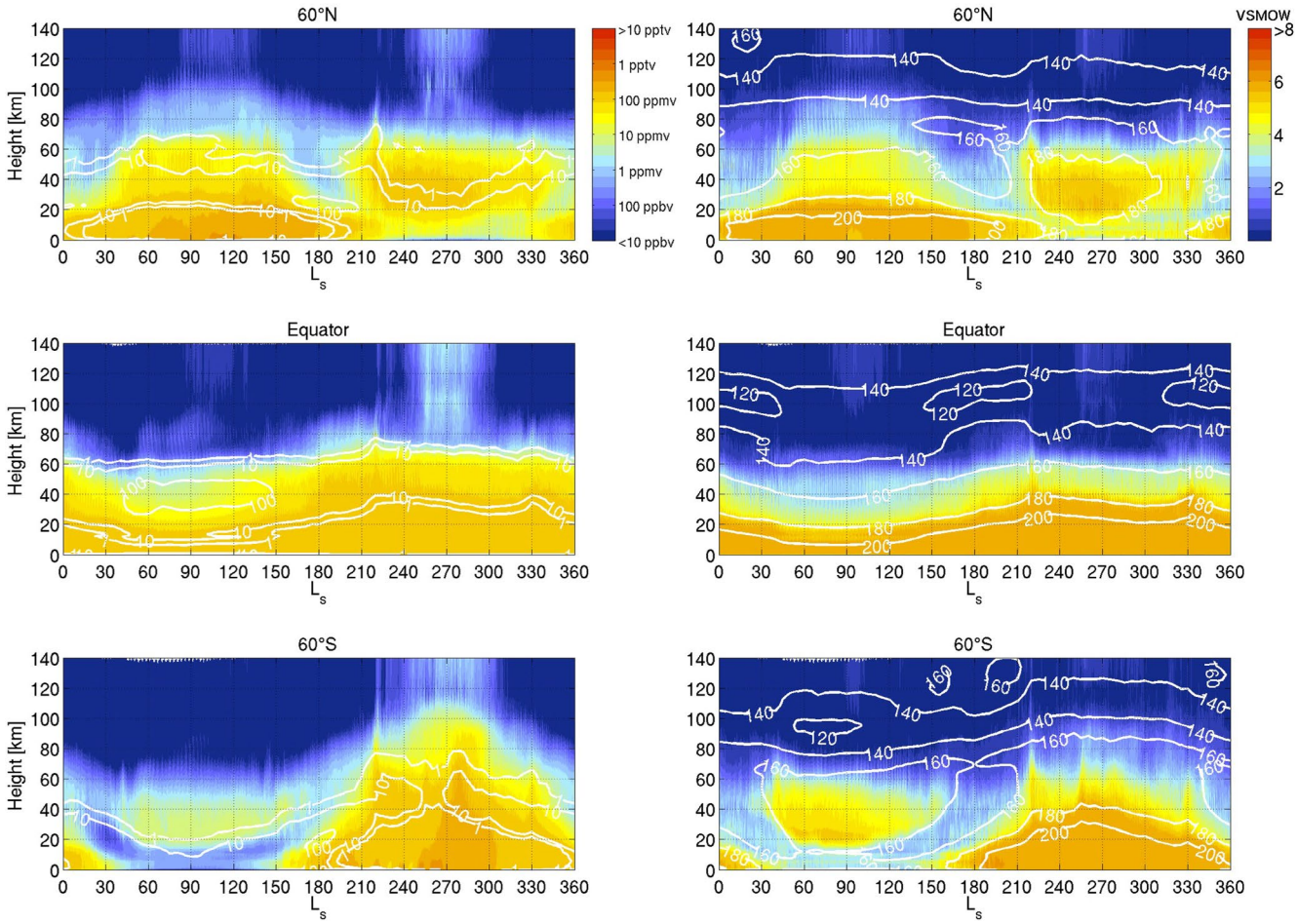

Figure 6. Seasonal variation of the zonal mean water vapor (left) and gas phase D/H (right) vertical profile at three latitudes. The simulation results were averaged over all longitudes and local times. The white contours are the ice water content (left, ppmv) and temperature (right, K) averaged over 5° L_s.

were discussed in the previous section (~5.7 × VSMOW). Without fractionation upon deposition of water vapor, D/H would remain constant all the way up to the upper atmosphere. Instead, above the clouds, it drops to below 1 × VSMOW with some seasonal variability. In the polar regions at equinox, and at the winter poles at solstice, the lower atmosphere also has low D/H values down to the surface, where also direct deposition to the surface contributes to strong water fractionation (see also Figure 3).

Seasonal variations in the D/H vertical distribution are governed by variations in cloud formation, which are imposed by the orbital forcing of the Martian climate, that is, they are temperature driven. For completeness, we show the simulated water ice clouds and the D/H ratio in the clouds in Figure 5. As expected, D/H is larger in the clouds than in the gas-phase.

In addition to these latitude-height cross-sections, we show time series of the water vapor and D/H vertical profiles at selected latitudes in Figure 6. It can be seen how the thick cloud level where the strongest water vapor decrease with height occurs, varies with season, driven by the seasonal variations in temperature. Again it can be seen that the D/H ratio drops more rapidly than water vapor, because of heavy fractionation in the clouds in this region. The simulated clouds (IWC) and the D/H ratio in the clouds are shown in Figure 7.

The variation of the height of the cloud layer with season and with latitude, implies that the D/H ratio in the gas phase is constant up to different heights throughout the year and for different latitudes, as was already mentioned before. This will be an important benchmark when comparing to vertically resolved D/H observations provided by TGO instruments.

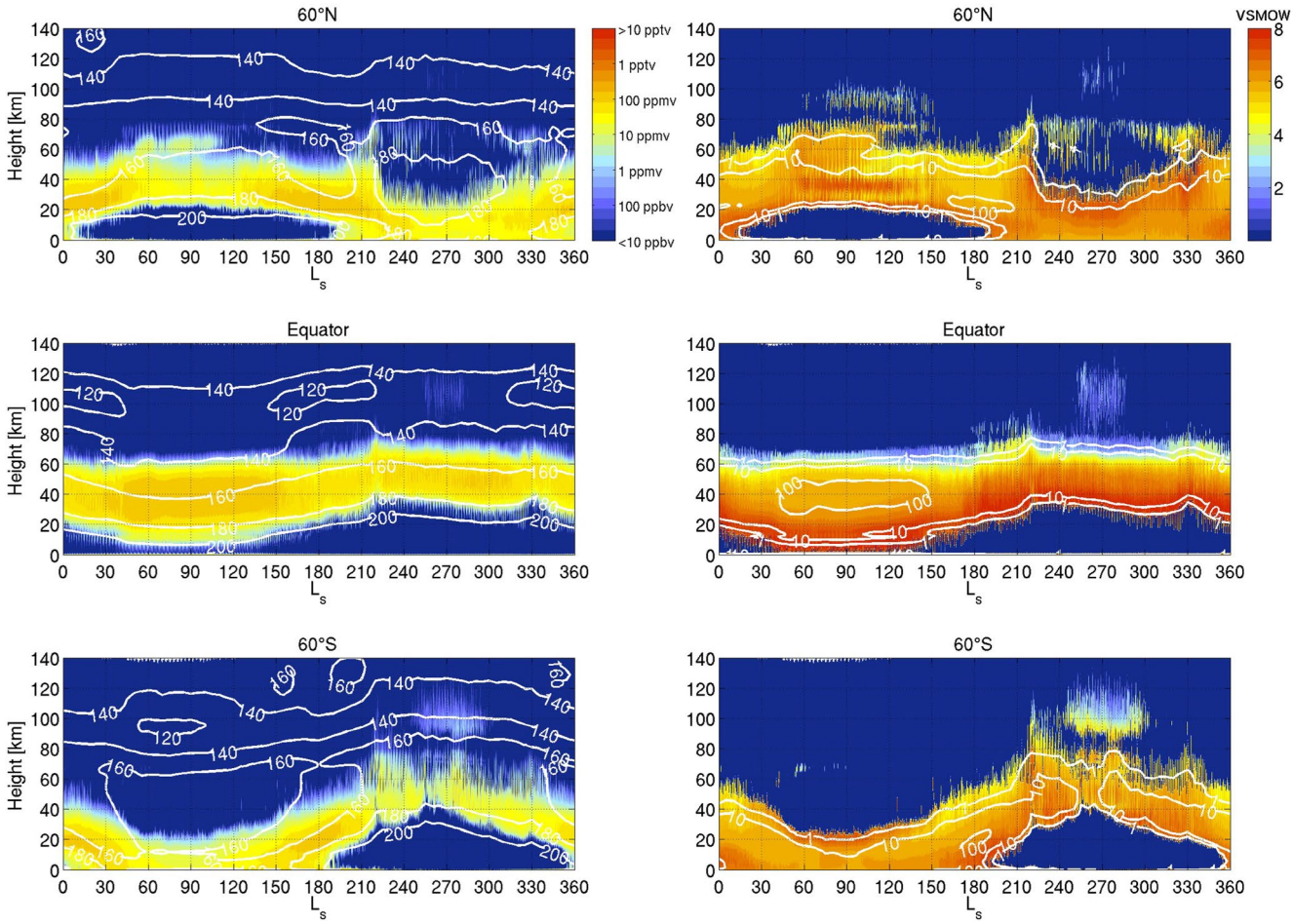

Figure 7. Same as Figure 6, but showing ice water content (left) and D/H in the ice phase (right). The white contours are the temperature (left, K) and ice water content (right, ppmv) averaged over 5° L_s.

3.4. D/H Simulation: Spatial and Diurnal Variability

In this section, we want to explore the level of variability in D/H on the spatial (horizontal) scale and the diurnal variability, both of which are strongly related. Figure 8 shows instantaneous horizontal maps centered at local noon, and spaced 45° L_s throughout the year of the total column D/H. The variations in the total column D/H are small and dominated by the seasonal trends already shown in Figure 2 and discussed in Section 3.2. The only remaining stronger D/H feature is over Olympus Mons (20°N and 135°W), where in particular in the period around $L_s = 90°$ the D/H value is below the planetary average. (To a lesser extent this is also the case over Arsia Mons.) This is the period of the ACB when there is a lot of cloud formation over Olympus Mons. Moreover, given its height, the total air mass above the top of the mountain is small, and local conditions have a stronger impact on the total column. The times of the maps of Figure 8 are so that Olympus Mons is in the nighttime, with strong cloud formation. This will be discussed more further down in this section.

Figure 9 shows the near-surface gas-phase D/H for the same conditions as Figure 8. During the night, strong ice deposition at the surface and low-level cloud formation remove a lot of HDO near the surface, and the D/H ratio drops down to 2–3 × VSMOW just before dawn almost everywhere. When the ice at the surface sublimates, the local near-surface gas-phase D/H increases and remains above average (>∼6 × VSMOW) for almost 2 hr into the daytime. These strong diurnal cycles in the lower atmospheric D/H are nevertheless too weak to be visible in the total column D/H.

To address the NOMAD vertical D/H profiles, which are taken from solar occultation measurements in terminator conditions, it is also important to look at the spatial and diurnal variability at higher levels. Figure 10 shows

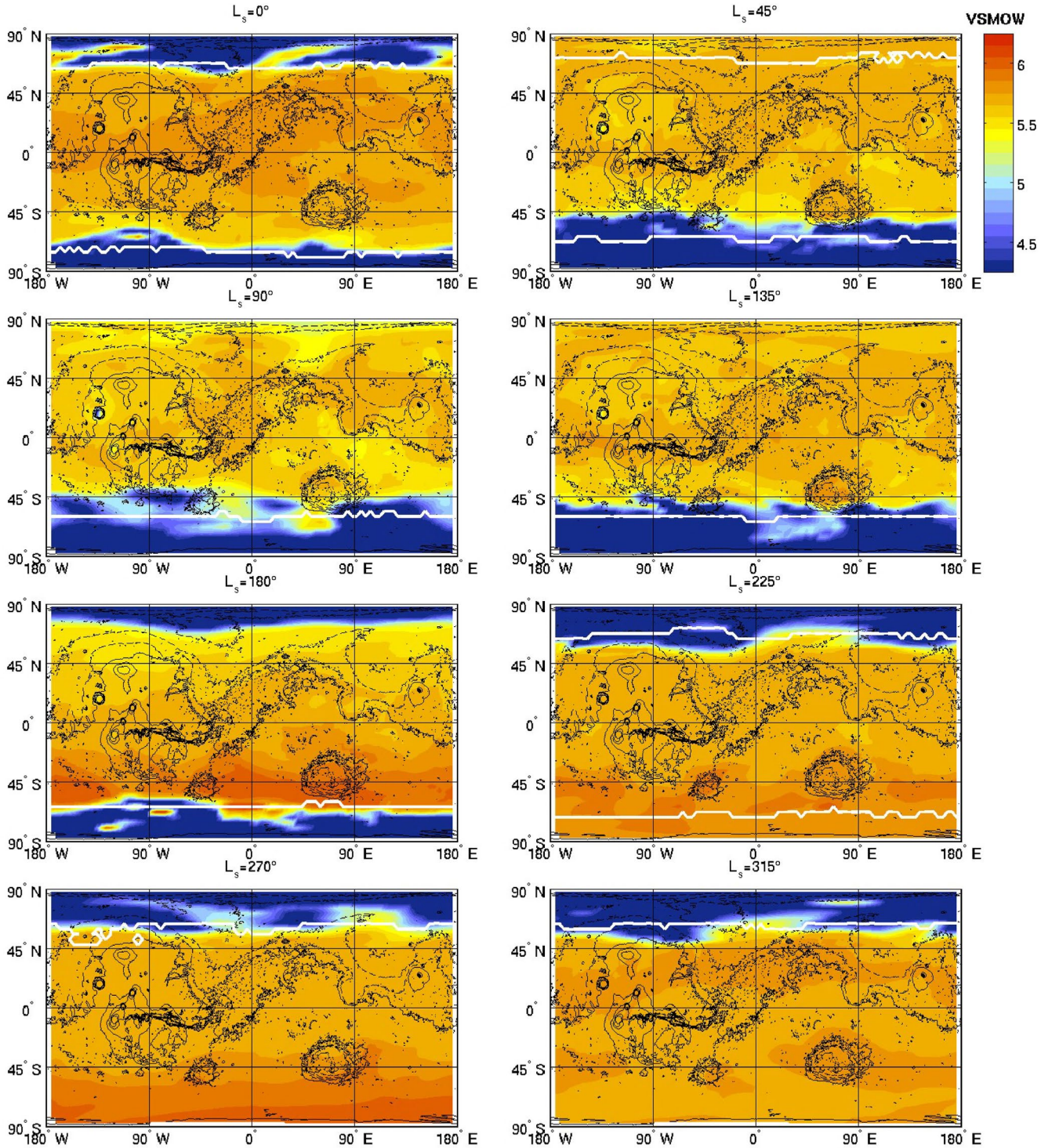

Figure 8. Horizontal maps spaced 45° L_s of the simulated HDO/H_2O total column ratio. Each map is instantaneous for local noon at 0° longitude. The white contour lines indicate the edges of the simulated CO_2 ice caps.

the average diurnal variation of the D/H profile for three latitudes (60°N, equator, and 60°S) for the four cardinal seasons. Averaged over 10 sols, and except for the near-surface (see Figure 9), the D/H ratio shows no diurnal variations in the lower atmosphere. The height of the layer where no diurnal variability is seen is however, varying with season, and is controlled by cloud formation. At the height of the strongest cloud formation, a strong diurnal

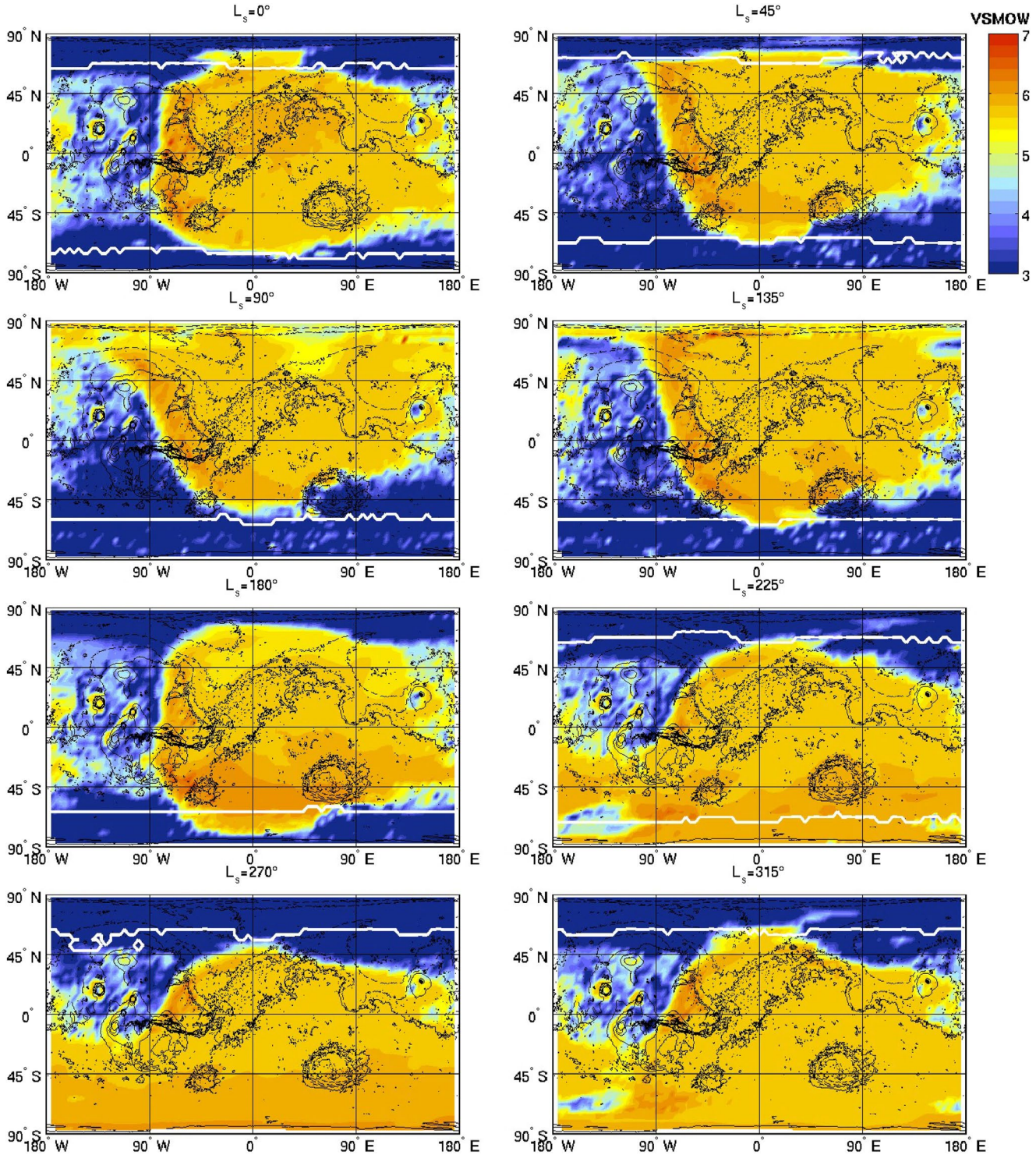

Figure 9. Horizontal maps spaced 45° L_s of the simulated gas-phase D/H ratio at the surface. Each map is instantaneous for local noon at 0° longitude. The white contour lines indicate the edges of the simulated CO_2 ice caps.

variability can be seen in almost all cases. NOMAD D/H observations are taken at the terminator (so ±6 and 18 hr local time) and range up to 60–80 km (see Section 5.2). So we can expect they will sample height ranges that are characterized by a strong diurnal variability in the model. However, the NOMAD D/H data set used in this paper covers only the second part of the year (L_s ~ 160°–360°), and in this time range, the model predictions are often

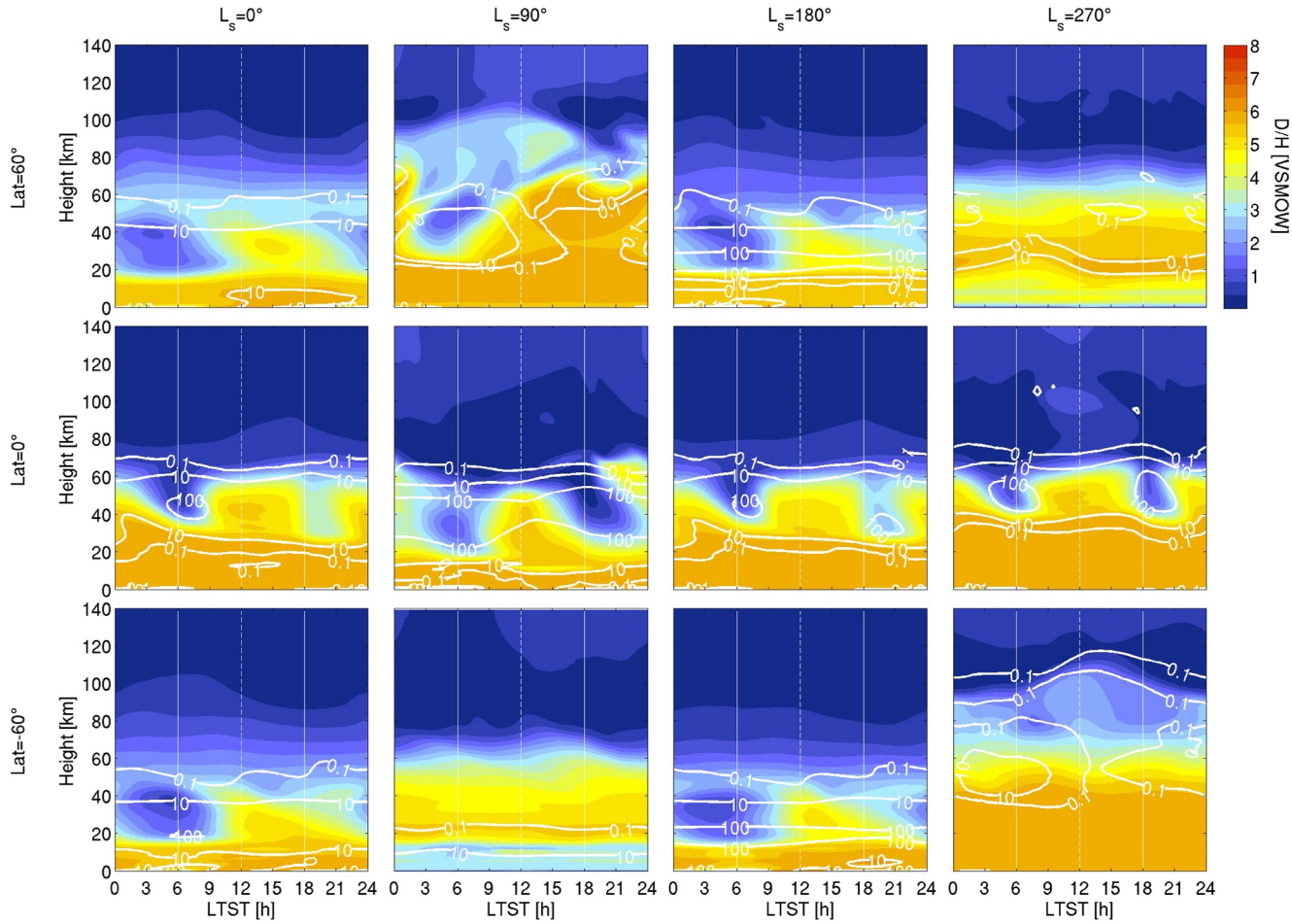

Figure 10. Diurnal variation of the gas phase D/H vertical profile at three latitudes for the four cardinal seasons. The diurnal cycle was averaged over 10 sols. Contours represent the ice water content (in ppmv). Full white vertical lines indicate the terminators and so the (approximate) time of the NOMAD solar occultation observations, the dashed white line is local noon.

quite symmetric between morning and evening terminators (Figure 10), so that this diurnal variability may not be recognized from the selected local time sampling. This will be further discussed in Section 5.2.

In Figure 11 the diurnal cycles of the gas-phase D/H are shown for a range of heights over a few example sites that are representative for a variety of location contexts: Olympus Mons (high topography), Hellas (low topography, south), Gale crater (the location of the Mars Science Laboratory (MSL), equatorial), and the location of the Phoenix lander (low topography, north). The diurnal cycle shown is for a single sol at each of the cardinal seasons. The D/H values shown are for total column, near-surface, and for 30 and 50 km altitude.

The column D/H ratio only shows diurnal variability at two locations in specific seasons. As already mentioned above, over Olympus Mons near aphelion ($L_s = 90°$), because of ACB related cloud formation, with drops in D/H from 5.5 down to 4.3 resp. 4.6 × VSMOW in the morning and evening. And, at the Phoenix site at times when it is covered by the seasonal CO_2 ice cap ($L_s = 0°$ and 270°), when the local water and HDO columns are small and hence sensitive to diurnal changes in ice formation.

The near-surface D/H ratio shows more variability at all sites, except during southern summer season ($L_s = 270°$) when only Olympus Mons shows a diurnal cycle. The day-night variations at Olympus Mons are persistent all year round. At low (MSL) and moderate (Hellas) latitudes, the near-surface diurnal cycle is the strongest around the aphelion season.

From these model predictions, it appears to be difficult to detect diurnal D/H variability on Mars in terms of total column observations, from Earth or from orbit without specific access to the near-surface atmosphere. We note

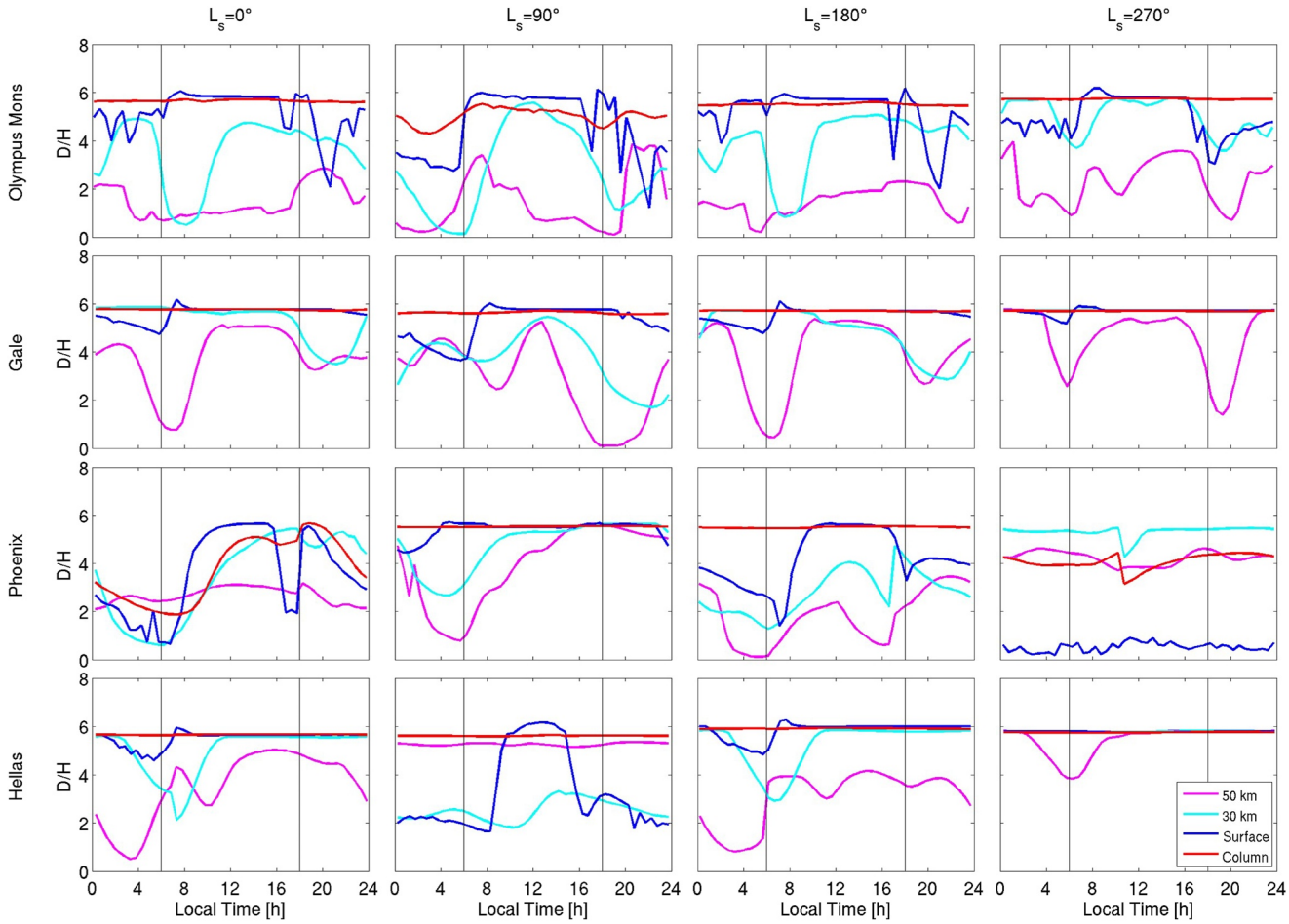

Figure 11. Diurnal variations of the gas-phase D/H ratio for the total column (red), at the surface (blue), at 30 km (cyan), and at 50 km (magenta) for one simulated sol at the four cardinal seasons, for four example locations. The vertical black lines indicate terminator conditions in the lower atmosphere (6 and 18 hr Local True Solar Time).

that photolysis induced hydrogen fractionation of water vapor (Yung et al., 1988) is not yet included in our model, nor is the differential escape of D and H atoms. However, given the abundances of water vapor and HDO in the lower and middle atmosphere, we expect these processes to have only an impact on the D/H variability in the upper atmosphere, and so not to show up in total column D/H (see also Alday et al. (2021) for a recent prediction on HDO photolysis). Also regolith adsorption is not yet included in our GCM simulations. It remains to be explored what additional impact adsorption-induced hydrogen fractionation of water vapor at the surface (Hu, 2019) would have on the diurnal variability of D/H in our GCM, and if the impact on total column D/H variability would be larger than in the present simulations.

3.5. Comparison to Other GCM D/H Simulations

To date only two other GCM studies of D/H simulations were published, both with the same model: the pioneering work of Montmessin et al. (2005, hereafter M2005), and the related work of Rossi et al. (2021, hereafter R2021). The small seasonal variations, the low values in the polar winters, and the lower values at southern latitudes in the aphelion season found in Figure 2 are also present in these works. The atmospheric mean D/H value is 5 × VSMOW in M2005 compared to 5.7 in our work. This value is controlled by the predefined D/H value in the permanent cap, which is 5.6 in M2005 and 6 in our work. The drop in D/H between the permanent cap and the atmosphere is much stronger in M2005 (15%) compared to our work (5%). We attribute this to the differences in cloud simulations with our work, and perhaps also combined with the refined water saturation pressure expression (see Section 2.1) and fractionation coefficient (see Section 2.2). Montmessin et al. (2004),

in their Figure 6, show zonal mean cloud optical depths up to 0.5 over the polar summer cap. These clouds are considerably thicker than in our simulations, where they do not exceed 0.1 in zonal mean (not shown). This will make the "isotopic filter" (as introduced in M2005) caused by polar clouds stronger in their work. Cloud water ice columns in our simulations (Figure 2, shown as contours on the middle plot) are comparable to those derived in Olsen et al. (2019), in particular in northern summer.

M2005 also show enhanced D/H values in southern summer, as our model confirms. But they also predict a similar enhancement in northern summer, which we do not see. This may again be a result of the differences in north polar summer clouds in both simulations. The vertical distribution of D/H for two seasons shown in Figures 6 and 7 of M2005, are qualitatively similar in our work (Figure 4).

Finally, M2005 find the southern residual cap as a strong loss for D/H, estimated at 0.5% per year. We do not find such a strong loss. To start with, our residual cap is much smaller than the one of M2005 (our cap being closer to the observed one, see Figure 1). But also the implementation of the permanent cap may play a role here, as we make a distinction between permanent and transient ices, with the D/H in transient ice being lower (Figure 3), making also the D/H from this source smaller.

R2021 apply the same model as M2005, with some model improvements, however, those seem not to strongly affect the results of M2005. Like us, R2021 also apply the updated fractionation factor of Lamb et al. (2017). Interestingly in their Figure 1, R2021 provide an analysis of the impact of using this new factor over the one previously used in M2005 (Merlivat & Nief, 1967). The result is that, at least for total column D/H, it only makes a difference in the polar winters, where the D/H values are somewhat increased when using the new factor, but not for the overall atmospheric D/H values, at least not for the D/H column.

An important difference between R2021 and M2005 is that in R2021, the permanent ice cap is initialized at 5 × VSMOW, so considerably lower than M2005 (5.6 × VSMOW), and than in our work (6 × VSMOW). But the resulting atmospheric D/H values in R2021 (their Figure 2) are similar to those of M2005 (see Figure S1 in the Supporting Information of R2021). An explanation for this is likely found in the different ways that M2005 and R2021 initialize their simulations. M2005 initialize them in the same way as we do, from a dry atmosphere, while R2021 initialize them with a fully spun-up water cycle, and with an overall D/H ratio of 5 × VSMOW, that is, exactly the same value as in the permanent cap. Such a set-up is less likely to result in decreasing atmospheric D/H, and could explain why the results in both papers are similar.

As before, we conjecture that the absence of radiative cloud feedbacks in M2005 and R2021 are the dominant factor explaining the differences of both works with our results, in particular the action of north polar ice clouds.

The simulations of R2021 for the GDS conditions will be discussed in Section 4.

3.6. Comparison to Historical In Situ and Earth-Based D/H Observations

In this section, we will discuss comparisons to previous D/H measurements.

3.6.1. Comparison to the In Situ Measurement

As mentioned in the Introduction, there is one in situ D/H measurement available, in addition to a long list of Earth-based observations. The only in situ reported measurement of D/H was done by the TLS-SAM instrument on MSL (Webster et al., 2013): δD = 4,950 ± 1,080, or D/H = (5.95 ± 1.08) × VSMOW. In their Supporting Information, it is explained that this is actually an average of two measurements: 4,420 ± 430 (D/H = 5.42 ± 0.43) on mission sol 73, and 5,480 ± 980 (D/H = 6.48 ± 0.98) on mission sol 79. Both sols are close to each other, 6 sols apart around $L_s \sim 192°$, and such a large change is not predicted by the model on such a short time scale. The simulated diurnal variation of the total column D/H at the MLS location in this season is small, but the local D/H value at the surface shows a fast variation in the morning of ~0.5 × VSMOW (Figure 11, MSL case for $L_s = 180°$, the closest to the reported measurements), which is within the 1σ error provided by TLS-SAM. The two TLS-SAM measurements were done at the same local times, close to midnight. This seems to exclude that the discrepancy between them is due to diurnal variability, unless there would be a considerable change in cloud formation between both sols that we could not verify. We note that our model fields were not corrected for the topography of Gale crater, and local conditions may be different than simulated in our GCM.

3.6.2. Comparison to Earth-Based Observations

The first ground-based observations of Mars D/H were reported in Owen et al. (1988) (L_s = 316°, global result: 6 ± 3 × VSMOW), Bjoraker et al. (1989; L_s = 246°, global result: 5.2 ± 0.2 × VSMOW), Encrenaz et al. (1991, 2001; L_s = 100°, global result: 6 (+6, −3) × VSMOW), and Krasnopolsky et al. (1997; L_s = 222°, low southern latitude, 5.5 ± 0.2 × VSMOW). Given the uncertainties in the retrievals, our simulations seem consistent with all these results.

Later observations could provide information over spatial ranges (longitude and latitude). We will discuss some of them in more detail, in chronological order of the related publications.

In 2011, a first report was made of the D/H observations by the team of Novak, Villanueva, and Mumma (Novak et al., 2011), an ongoing effort which finally evolved to the work of Villanueva et al. (2015). The observation reported in Novak et al. (2011) from CSHELL, NASA-IRTF at L_s = 50° is interesting because it covers all latitudes (except the south polar winter). The decrease of D/H at southern and at high northern latitudes is similar in our simulation. But the reported low latitude values are relatively high (5.5–7 × VSMOW), where our model with its current settings gives ∼5.7 × VSMOW (which is 14% above the Montmessin et al. (2005) result that had to be scaled in Novak et al. (2011)).

Krasnopolsky (2015) presented latitude-resolved D/H observations obtained between 2007 and 2014. They also include a comparison to the GCM results of Montmessin et al. (2005), which are ∼12% lower than our results (see Section 3.5). In Krasnopolsky (2015), we see that the observations in their Figures 3 and 5 are below the GCM prediction of Montmessin et al. (2005), and will also be lower than our results. For their Figure 4, the observation is closer to our prediction. The observation reported in their Figure 8 is also above the prediction of Montmessin et al. (2005), but in northern latitudes becomes high, up to 8 × VSMOW, values we never see in our simulations. Finally, for their Figure 10, there is a good match with the Montmessin et al. (2005) simulation. But the reported variability and errors are large.

Aoki et al. (2015) performed several latitude-resolved D/H observations from the Subaru telescope, at L_s = 52° and 96°. The D/H values were centered around ∼4 × VSMOW, and decreased toward higher latitudes for L_s = 52°, but not for L_s = 92°. Our simulations are higher than these observations on all occasions, but remain often within the large observational error bars. The model predicts no significant latitude trend except for the high polar latitudes that are not covered by the observations.

Villanueva et al. (2015) reported horizontally resolved maps of D/H derived from several observations between 2008 and 2014. Overall, our atmospheric D/H values are lower than those reported in Villanueva et al. (2015), which also show a much larger range. The strong horizontal D/H variability reported in some of the observations is not reproduced in our simulations, yet the observed variability could be attributed to the existence of clouds/dust, which hides the underlying full column. (For a discussion about spatial and diurnal variability, we refer to Section 3.4.) In general, the north-south D/H gradient, at least qualitatively, corresponds to what the model predicts in Figure 2 (top) and Figure 8, with a decrease toward southern latitudes for the aphelion season and toward high northern latitudes for the second half of the year.

Encrenaz et al. (2016, 2018) also provided full maps of D/H observed using the EXES telescope on the SOFIA airplane on three occasion: 8 April 2014 (L_s = 113°), 24 March 2016 (L_s = 127°), and 24 January 2017 (L_s = 304°). The resulting disk-averaged D/H ratio was respectively 4.4 (+1.0, −0.6), 4.0 (+0.8, −0.6), and 4.5 (+0.7, −0.6) × VSMOW, on all occasions below our model results. However, the resolved maps showed some more variability. On the first case, the dominant value was close to 5 × VSMOW, with only deviations to lower values at low southern latitudes, as expected by the model. Higher values were only measured near the northern rim. In the second case, a more uniform map was found with a D/H mostly between 4 and 6 × VSMOW, in accordance with the model. For the third case, because of the small apparent Mars diameter only a line plot was provided, with D/H weakly decreasing from ∼5 × VSMOW in the north to ∼4.5 × VSMOW at high southern latitudes. As with the observations of Villanueva et al. (2015), while the absolute values are not always matching the model results, often the latitude trend is as the model predicts.

Khayat et al. (2019) report latitude-resolved D/H observations taken on 21 March 2016 (L_s = 126°), for a range of longitudes. For three of these observations, the reported D/H values are rather low (2–4 × VSMOW), and below our model results. The observations for longitudes 236° and 253°W are higher only in the northern latitudes

(~5 × VSMOW) and closer to our simulations. The model also does not predict such a strong decrease for southern latitudes (somewhat similar to that reported in Villanueva et al., 2015), but only a moderate decrease starting from 30° to 40°S latitudes.

In conclusion, the various reported column-integrated observations show a wide variability, which in many cases highlights the challenges of measuring the total column of water and HDO from nadir/observatory measurements in an aerosol-rich and optically thick environment. The existence of clouds and dust particles in the Martian atmosphere can mask a large fraction of the column, in particular for water, which is mostly concentrated in the lower scale heights. Yet, these observations generally show similar latitudinal trends as described by the model, and we think that our simulations fall within the range around the overall average of all these ground-based observations. Complementary to these maps of column water and D/H, orbital solar occultation observations provide vertical information of the distribution of water and D/H. Although with lower spatial mapping potential, such measurements permit sensitive probing of the atmosphere and a direct characterization of the aerosols in the column. The first sensitive detections from orbit (Villanueva et al., 2021) will assist to understand how performant our simulations are. These comparisons will be presented and discussed in Section 5.

4. Impact of the Global Dust Storm

Within the first year of the NOMAD observations, a large GDS, or A-storm (Kass et al., 2016) occurred, between L_s = 190° and 240° (Montabone et al., 2020). Later that year also a RDS, or C-storm occurred between L_s = 320° and 330° (Montabone et al., 2020). While we will analyze both storms later on in this paper, here, we will focus on the GDS. NOMAD and ACS solar occultation observations indicated that a strong redistribution of water vapor to high altitudes and latitudes took place during the GDS (Aoki et al., 2019; Fedorova et al., 2020; Vandaele et al., 2018). However, there were no observations available in the similar season in a year with no GDS. Such results are being prepared at the time of submission of this paper. But GCM modeling using the GEM-Mars model for the time of the GDS, and for a non-GDS year, provided the theoretical insights (Neary et al., 2020) that confirmed such a redistribution of water vapor during a GDS. Given the strong dependence of the D/H distribution on that of water vapor, it is important for the present paper to also investigate the behavior of HDO and D/H in GDS conditions.

As explained in Section 3.1 and Neary et al. (2020), we will do such simulations using the dust climatology for MY 34 (Montabone et al., 2020), and compare this simulation with a typical non-GDS year, in this case MY 33. To constrain the total optical depths, the dust climatology v2.3 of Montabone et al. (2020) was used. (Version v2.3 contains only daytime dust abundances, but for the more evolved climatology (v2.5) that includes diurnally variable dust, there is no similar version for the other years available.) Figure 12 shows the actual scenarios used in the simulations as contours. As also explained already in Section 3.1, during the GDS (actually for the period L_s = 160°–230°) and RDS (315°–330°), the vertical distribution of dust was prescribed by a Conrath vertical distribution (Conrath, 1975), with ν parameter (controlling the vertical profile shape) as defined in Section 3.1, dependent on the total dust optical depth.

The simulations predict only a limited impact of the GDS on the total columns of H_2O and HDO (not shown), and so also on the column D/H (Figure 12). Figure 13 shows the simulated impact of the GDS on the D/H vertical distribution over time, for three selected latitudes (high north and south, and equator). At all the latitudes there is a strong uprise of D/H to ~60 km height during the early phases of the GDS, due to atmospheric warming by the dust and the decrease of ice cloud presence in the lower atmosphere (the effect was described in detail in Neary et al., 2020). This effect persists until L_s = 230° when the normal situation resumes.

Figure 14 shows the simulated redistribution of D/H across latitude as the GDS develops. For water vapor, a corresponding figure was shown in Neary et al. (2020, their Figure 3). It showed that during the GDS, water vapor is redistributed to higher altitudes and latitudes than in the normal case. For D/H, similar behavior is found, as HDO ascends with H_2O and there is no fractionation, since the clouds are supressed due to a warmer atmosphere caused by solar heating of dust in the GDS. During the early phase of the GDS, the lower atmospheric bulk value of ~5.7 × VSMOW is maintained up to ~35 km in the normal case, but goes up to ~55 km during the GDS. Also it extends to higher southern latitudes and all the way to the pole, and to 60°N latitude for the full height range to almost 60 km.

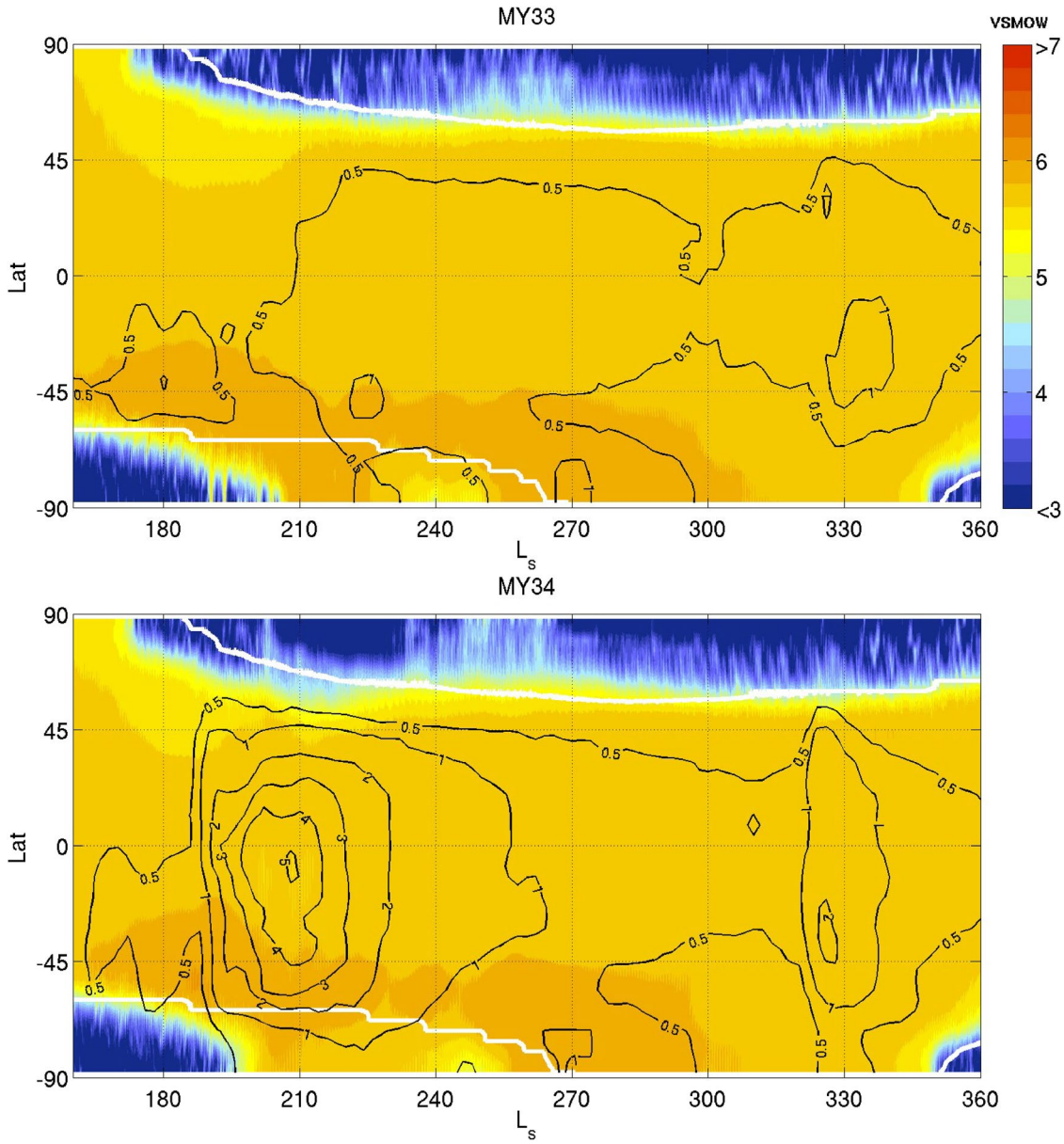

Figure 12. Zonal mean D/H column ratio as simulated in the standard (MY33) and MY34 simulations. The black contours are the zonal mean dust optical depths (at 0.67 μm and scaled to 610 Pa) from the scenarios used in both simulations (from Montabone et al., 2015, 2020). The white contour lines show the calculated edges of the seasonal CO_2 polar caps (zonal mean CO_2 mass exceeding 10^{10} kg).

We note here that when the model dust profiles are used without imposing a Conrath shape during the GDS, it will show the same effect during the GDS, but less strong (not shown). So it will redistribute water vapor and D/H not as high as in the Conrath profiles simulation. This was already shown and explained in the Neary et al. (2020) paper, and was exactly the reason why the Conrath profile shape was introduced in the model for dust storm conditions. As was discussed in Neary et al. (2020), the most likely cause for this is that the model currently lacks a parameterization for subgrid scale non-local deep convection (e.g., Heavens et al., 2018, 2019).

Our prediction for the behavior of D/H during the GDS is qualitatively similar to that of Rossi et al. (2021), although the effect seems to be stronger in our simulations.

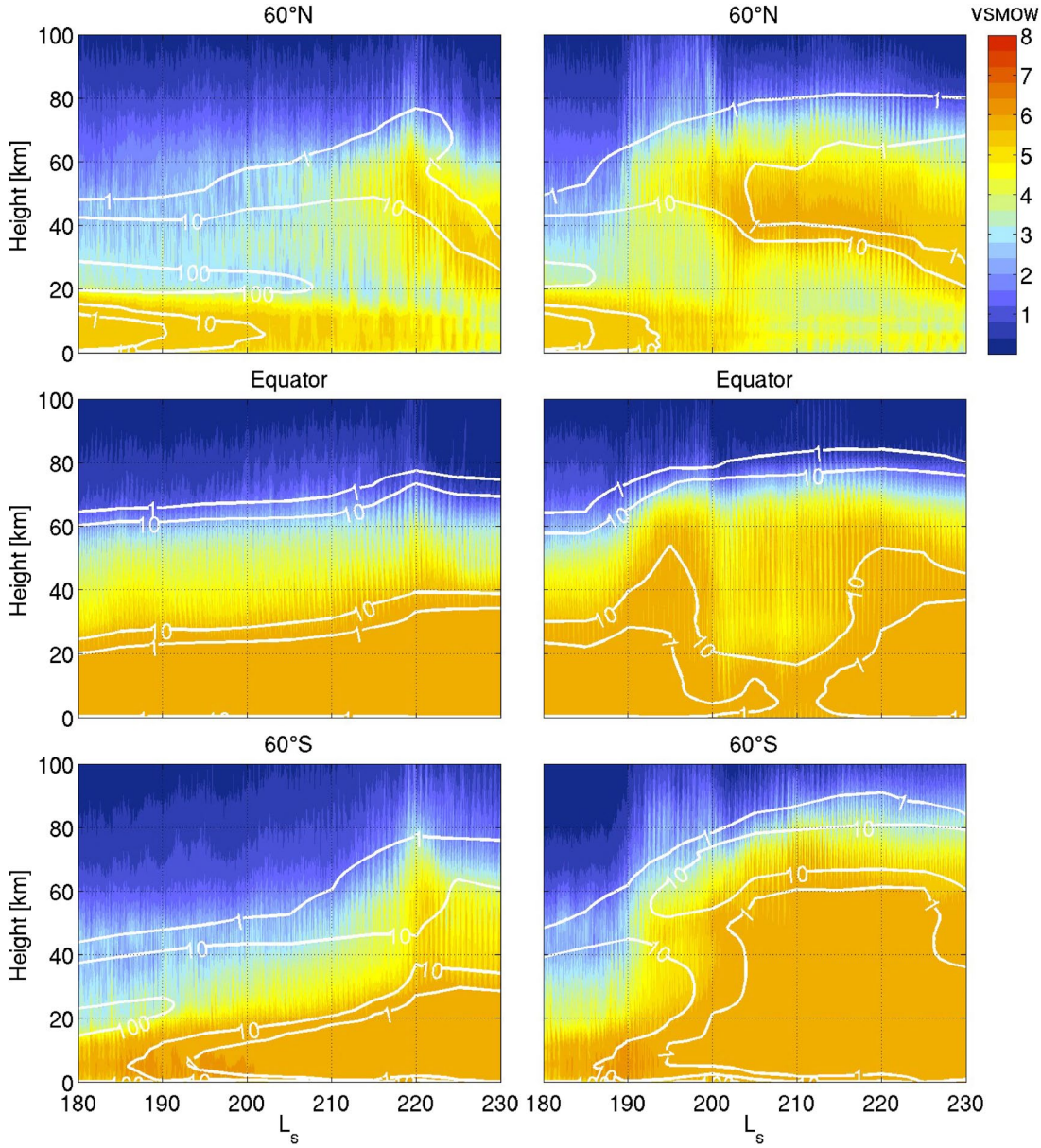

Figure 13. Simulated impact of the Global Dust Storm (GDS) at selected latitudes. The figure shows the time evolution of the zonal mean vertical distribution of the D/H ratio using MY33 dust (no GDS, left) and using MY34 dust (with GDS, right). Contour lines show ice water content binned over 5° L_s (ppmv).

5. Comparison With NOMAD Vertical Profiles

5.1. NOMAD D/H and Ice Cloud Data Set

The vertically resolved data set of D/H in water vapor retrieved from NOMAD solar occultations was first presented in Villanueva et al. (2021). Here, we repeat some of its main features. It is important to keep in mind the spatio-temporal distribution of the data set. As shown in Figure 15, the location of the solar occultation observations varies strongly in latitude over time. The sampling across longitude is rather uniform (not shown). It is important to be careful when mixing observations that are taken at different latitudes and times, as these will often be in different dynamical regimes and physical conditions. Some care has also to be taken when looking into the data themselves before doing any model comparisons. The data set is highly variable and sometimes shows large errors. These errors grow larger near the top of the retrieved profiles, where often they become much larger than 100% (see Villanueva et al., 2021 and their Supporting Information). We applied the following filters to the data:

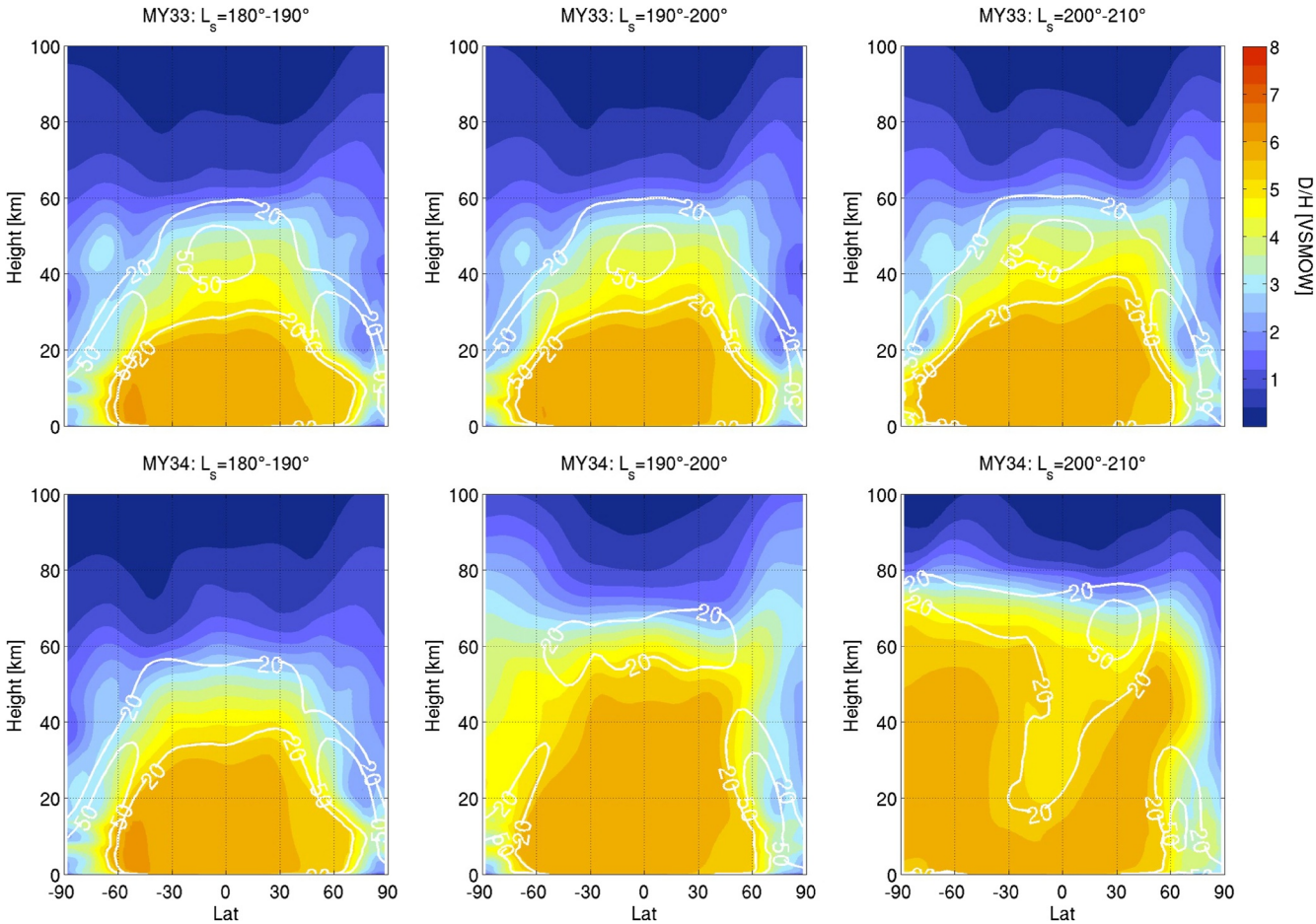

Figure 14. Simulated impact of the Global Dust Storm (GDS) on the D/H ratio in water vapor. The figure shows the latitude-height zonal mean vertical distribution of the D/H ratio simulated using MY33 dust (no GDS, top) and using MY34 dust (with GDS, bottom). The simulation results were averaged over all longitudes and local times and over (from left to right) L_s = 180°–190°, 190°–200°, and 200°–210°. Contour lines show ice water content (ppmv).

data are not retained in the comparisons when the reported retrieval error exceeds 2.5 × VSMOW or when they are larger than the retrieved value (whatever is smaller). Values that equal zero or exceed 10 × VSMOW are also removed. This leaves 49,704 individual retrievals for the comparison, in 1,490 out of 1,818 profiles with at least one useful data point.

For the interpretation of model-data differences for D/H, it is instructive to look into the role of water ice clouds, which are the cause of fractionation as considered in the model. To this end, we use the water ice MMR data set retrieved from NOMAD solar occultation observations by Liuzzi et al. (2020). We briefly summarize its main features. This data set consists of 1,793 profiles retrieved from mostly the same solar occultations and in the same time window as the D/H data set of Villanueva et al. (2021). Liuzzi et al. (2020) not only retrieve ice MMR but also dust MMR and particle radii for dust and ice. Here, we focus on ice cloud presence and so only on the ice MMR results. The data set also shows strong variability and so some filtering was also applied here, following the recommendations of Liuzzi et al. (2020). This leaves 55,705 individual values. Many of these profiles are co-located with the D/H retrievals, that is, they were retrieved from the same solar occultations (yet in a different pipeline). We performed a cross-check of the data sets, and for each profile in the D/H data set, we searched for a corresponding profile in the Liuzzi et al. (2020) data set (possible including zero ice MMR). For 135 out of the 1,490 D/H profiles (so <10%) that we retained after filtering, we did not find a corresponding profile, leaving 1,355 matching profiles with both D/H and ice MMR retrievals.

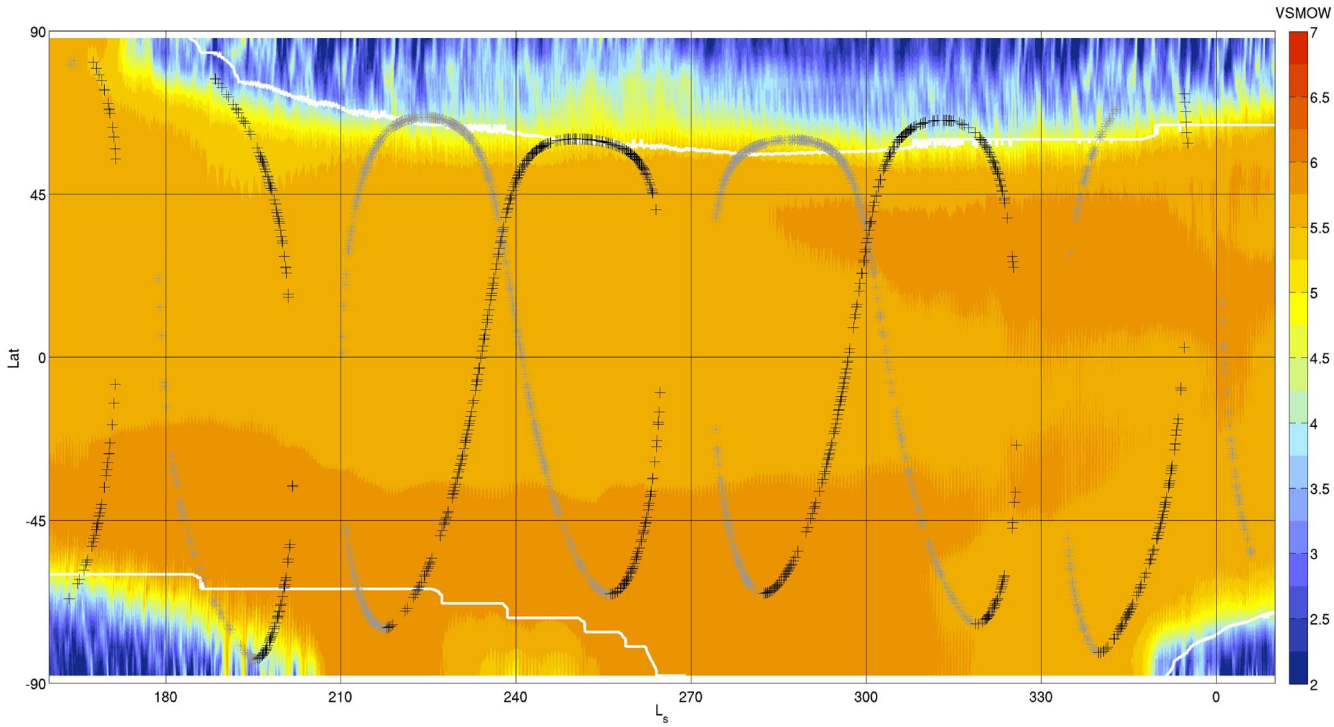

Figure 15. Overview of the L_s-latitude distribution of the NOMAD D/H observations. Gray stars are morning observations, black crosses are evening observations. The background contour shows the simulated column D/H and is the same as in Figure 12 (bottom).

5.2. Overview of Observations and Simulations

In the following model-data comparisons, we will look at two different simulations that were introduced earlier in this paper. One is for a non-GDS year, which is the one presented in Section 3, and which we chose to be MY33 (but can be considered as a climatology for a typical non GDS year), hereafter called the *standard simulation*. This will be compared to the simulation of MY34 (presented in Section 4), during which the observations were taken, and in which the 2018 GDS and RDS took place. The simulation results were interpolated in space and time to the NOMAD profiles, to within half a model time step (~15 min) accuracy.

Figure 16 shows an overview of all NOMAD D/H observations and the co-located simulation results for MY34, grouped in three wide latitude bands: 90°–45°N, 45°N–45°S, and 45°–90°S. This choice was made as a compromise between keeping this overview figure simple, minimizing the mixing of data taken at different latitudes, and maintaining a sufficiently dense temporal coverage of the profiles. The shown simulation results are the full model profiles at the average profile locations. This allows to see the model prediction of D/H toward the surface and toward the top of the atmosphere, beyond where NOMAD could observe, and puts the observed profiles in a wider context.

The added contours show the simulated ice MMR from the MY34 simulation, averaged over all latitudes, longitudes and local times within the three wide latitude bands. These contours indicate general trends in the simulations that are useful to understand the context of the individual observations. For a more detailed interpretation of the results, a comparison with the NOMAD ice MMR data is shown in a similar set-up in Figure 17. Here the contours show the simulated temperature from the MY34 simulation, also averaged over all latitudes, longitudes and local times in the three wide latitude bands. The strong correlation of cloud formation and of the D/H ratio (Figure 16) with temperature is apparent.

Figure 18 shows comparisons between the data and the two simulations, averaged over wide L_s-latitude bins. To allow for a proper average of all profiles in such bins, an altitude grid with respect to the MOLA areoid (Smith et al., 1999) and with a uniform spacing of 2 km was used everywhere, and all observations and co-located model results were binned into this 2 km altitude grid. The altitude with respect to the areoid was used as a common reference for all observations, as wide latitude bins can cover large variations in topography. Finally, the average

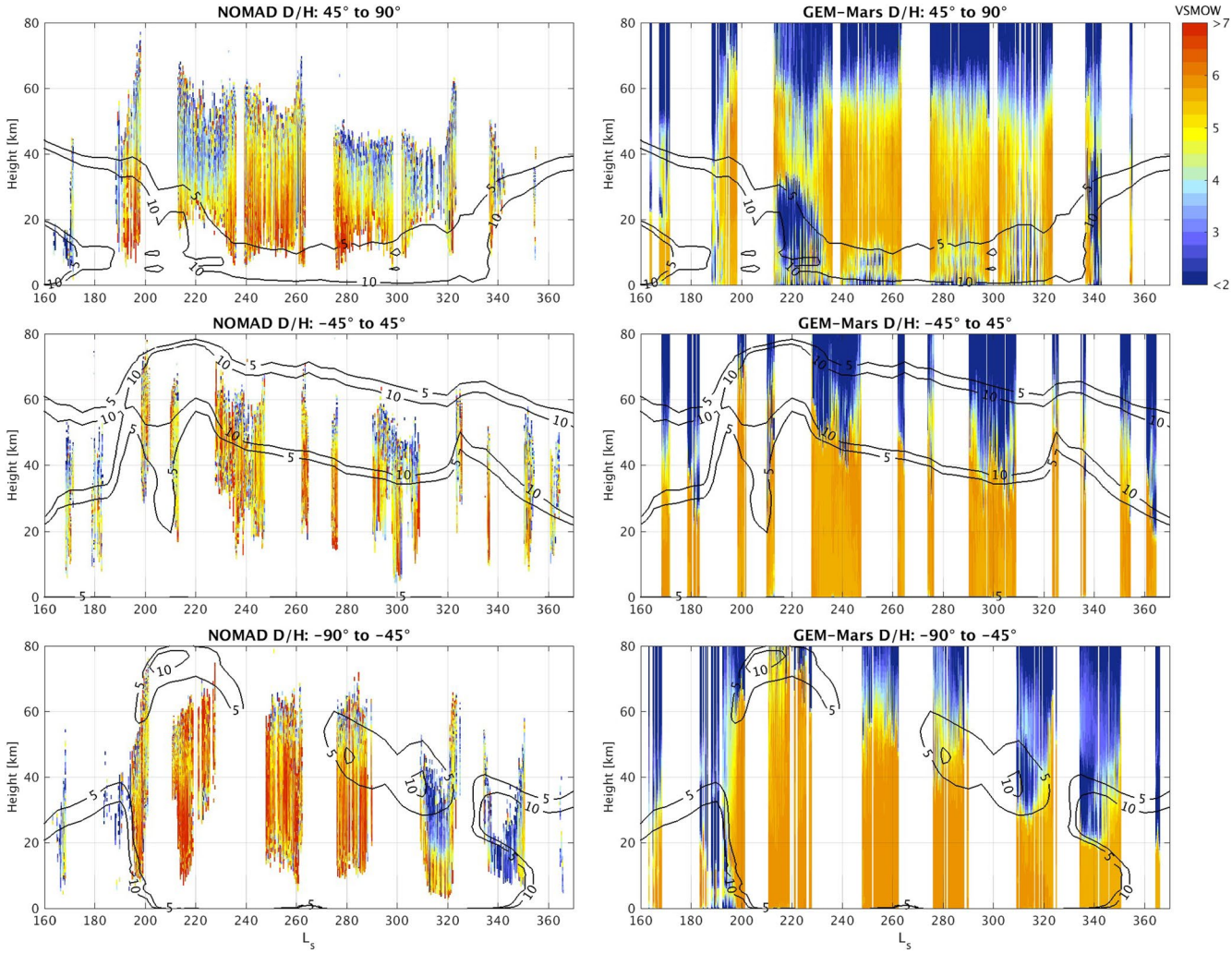

Figure 16. Overview of NOMAD D/H observations (left) and model simulations (right, MY34 simulation) in three wide latitude ranges. The simulation output was interpolated to the time and location of the observations. The black contour lines show the simulated zonal mean ice mass mixing ratio (in ppmm), averaged over the respective latitude ranges, over all local times and over 5° L_s.

and standard deviation within each level of this altitude grid was computed in each of the L_s-latitude bins, together with the standard error. Again, we plot the full GEM-Mars profiles at the average profile locations. Also the observed and simulated ice MMR are shown, which were treated in the same way as the D/H profiles. To keep the figure readable, only the ice cloud simulations for MY34 are shown.

5.3. Comparing Observations and Simulations

Figure 16 shows that overall the match between simulations and observations is good, both in terms of absolute D/H values and in terms of variability over time, latitude and altitude. In particular, the height range of the observed D/H finds an explanation in the simulations, as the top of the retrieved profiles is always close to where the simulated D/H drops strongly with height. Above this, HDO is no longer detectable. Figure 18 shows that the MY34 simulation generally remains within the variability and standard error of the observations almost everywhere.

In Figure 16, at mid- and southern latitudes, the added average model contours show that the D/H ratio is strongly reduced where ice clouds form. The temperature contour added to Figure 17 indicates the strong correlation of not only the cloud formation, but also the drop-off height of D/H, with temperature. At high northern latitudes, a decrease in the simulated D/H occurs at low heights as a result of near-surface cloud formation. This is consistent

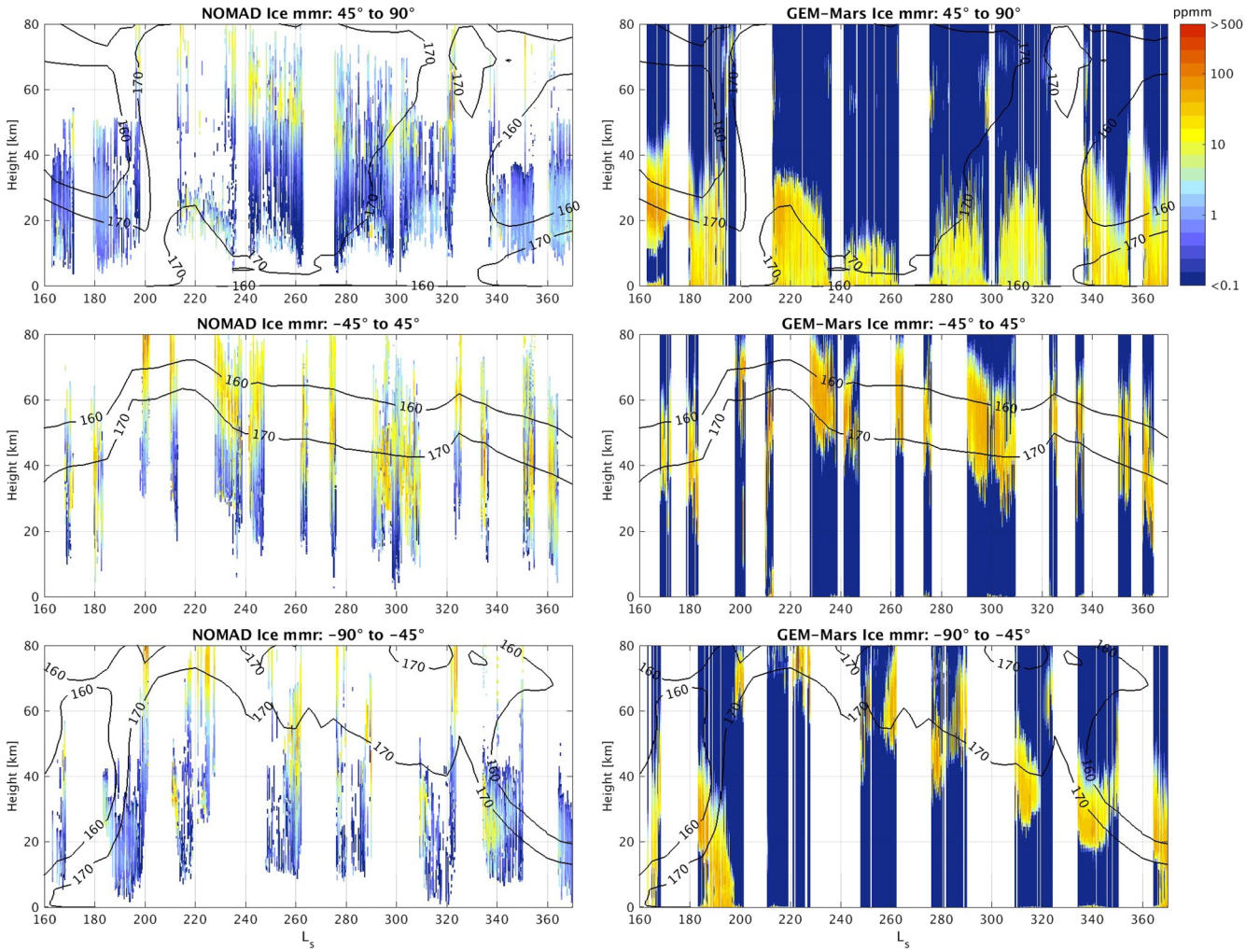

Figure 17. Same as Figure 16, but for the ice mass mixing ratio observations (left) and simulations (right). Here, the black contour lines show the simulated zonal mean temperature (in K), averaged over the respective latitude ranges, over all local times and over 5° L_s.

with the lower cut-off of the observed D/H profiles at these latitudes, which follow the simulated cloud contours always, except for the GDS when the local conditions are different from the global average. At larger heights, D/H rich air is transported in from lower latitudes, explaining why the D/H ratio increases again above the cloud level (see Sections 3.3 and 4, it is useful to compare this figure to the general model results of Figures 4, 6, 13 and 14).

Model-data biases in the D/H ratio can be noticed on some occasions (Figure 16). At high northern latitudes, the simulated D/H ratio is high compared to the observations below 20 km for L_s = 160°–170°, and above ~30 km for L_s = 280°–320°. In both cases, this bias can be related to an underestimation of the ice clouds in the model (Figure 17). On the other hand, between L_s = 215°–230° and below 30 km, the simulated D/H ratio is very low, due to excessive cloud formation in the model at this time (Figure 17).

At high southern latitudes near the end of the Martian year, the simulated D/H ratio remains high compared to the observations up to 30 km for L_s = 310°–320°, and up to 20 km for L_s = 330°–350°. While the pattern of intrusion of low D/H values from above to lower heights is similar to the observations on both occasions, it does not go as low as observed. Model cloud contours indicate that the simulated clouds remain too high in this season. This is confirmed by Figure 17, where clouds are observed at lower heights than simulated on these occasions.

Figure 18 shows the differences between the standard and MY34 simulations. These are found mainly in the second L_s bin (195°–230°), that is, during the GDS. There is a strong improvement at southern and low- to mid-latitudes when changing from the standard to the MY34 simulation. At southern latitudes the MY34 simulation

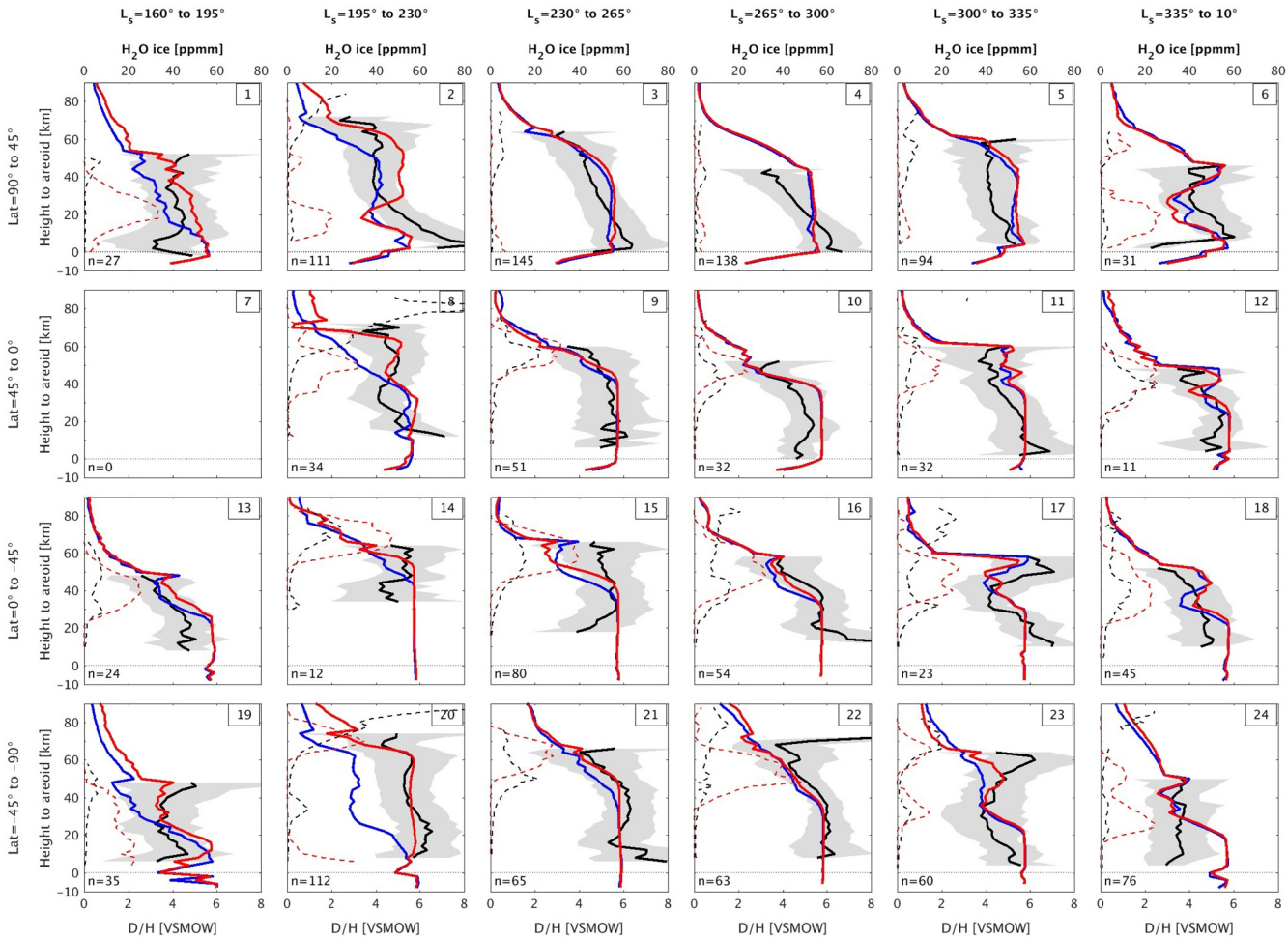

Figure 18. Comparison of NOMAD D/H (bottom scale) profiles (solid, black) and simulations (solid; blue: standard; and red: MY34) averaged over 35° wide L_s bins, 45° wide latitude bins and 2 km thick height bins. Gray shaded areas represent the variability of the observations (1σ variability + mean error of the observations). The numbers in the lower left corners indicate the number of profiles that were averaged in each frame. Dashed lines show the ice mass mixing ratio (top scale) observations (black) and MY34 simulations (red), co-located with the D/H profiles and averaged in the same way.

matches the observations almost exactly. This confirms the prediction of Figure 14 that the D/H ratio is strongly increased with height at high southern latitudes during the GDS. At low- and midlatitudes, the predicted increase of D/H above 40 km also leads to a good match with the observations, while below 40 km the observations are limited in height by the severe dust loading during the GDS. In the MY34 simulation during the GDS, the height at which the D/H drops is higher than in the standard simulation, and corresponds to the top height of the NOMAD profiles. This is consistent with the prediction of Figure 13, that is, HDO can be detected up to higher altitudes in the GDS.

During the perihelion/southern summer solstice season (L_s = 230°–300°), there is no significant difference between the two simulations, and almost everywhere both have a good match with the data at all latitudes. Only at high northern latitudes there is a small overestimate of D/H in the model between 20 and 60 km. This was already discussed above and can be attributed to insufficient high altitude cloud formation in the model. Finally, the impact of the RDS (L_s = 320°–330°) can be seen in the L_s = 300°–335° bin. It is much smaller than that of the GDS, and only visible at high southern latitudes between 30 and 60 km.

5.4. Local Time Variations

Section 3.4 showed that the model predicts sometimes altitude-dependent variability in D/H between the morning and evening terminator. To investigate this, Figure 19 shows averaged observed and simulated (MY34) D/H and

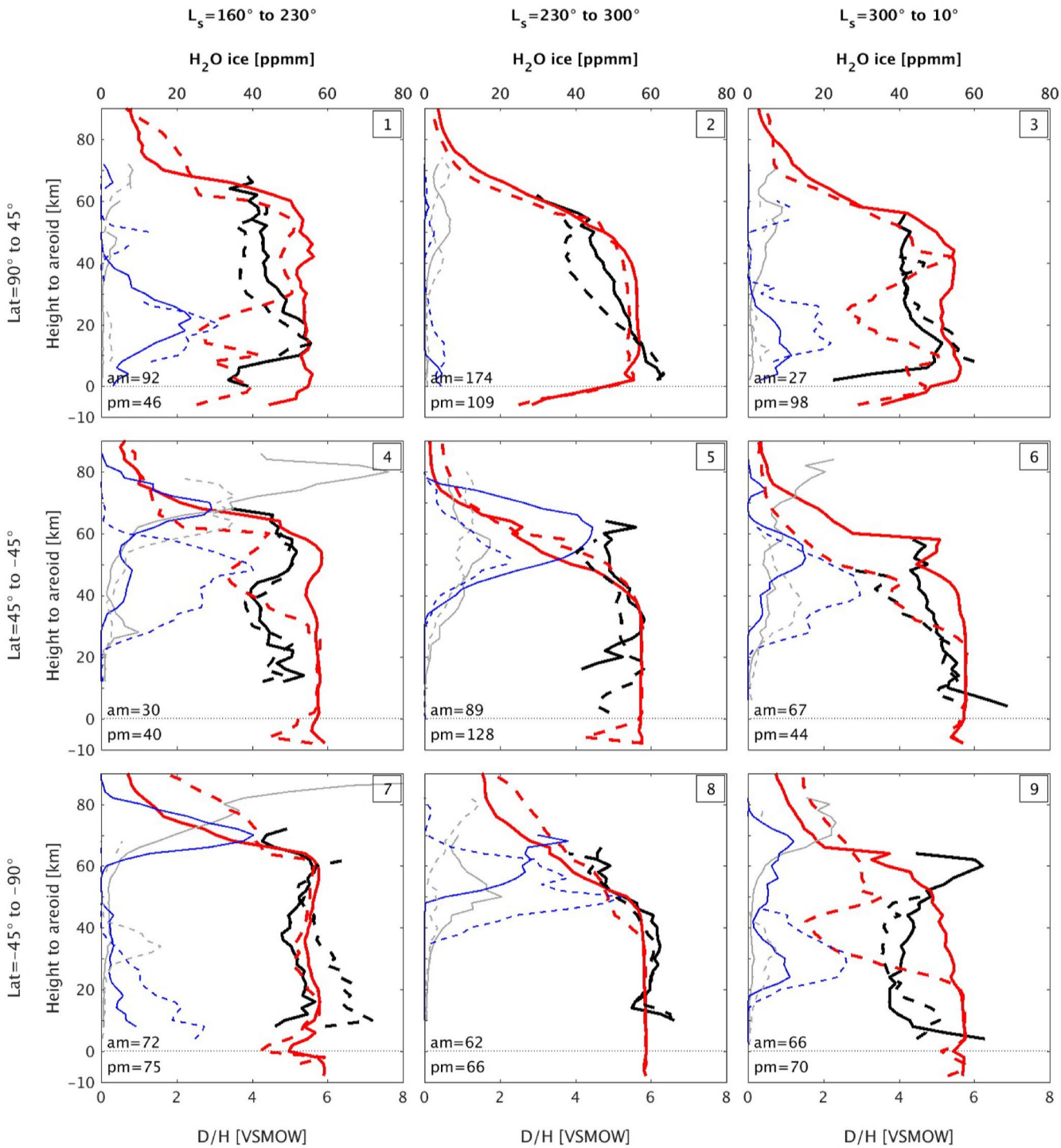

Figure 19. Comparison of NOMAD D/H (bottom scale) profiles (black) and MY34 simulations (red), separated for morning (dashed) and evening (solid) profiles, averaged over 70° wide L_s bins, latitude bins as indicated, and 2 km thick height bins. The numbers in the lower left corners indicate the number of profiles that were averaged in each frame. Overlaid are ice mass mixing ratio (top scale) observations (gray) and simulations (blue) co-located with the D/H profiles and averaged in the same way (morning: dashed and evening: solid).

ice MMR profiles in 70° wide L_s bins, with separation of morning and evening profiles (defined as mean local time of the profile before or after 12 a.m. local time). In almost all cases the difference between the observed morning and evening D/H is small, and smaller than the variability of the data themselves (this variability was

shown in Figure 18). An interesting difference between the morning and evening profiles in the observations is their upper retrieval cut-off. This is consistently lower in the morning profiles. This is likely because of the atmospheric expansion during daytime.

The simulations often show morning-evening differences of the same (small) magnitude than the observations, and within their variability. The only exceptions occur around the equinoxes, when the simulations show some located stronger morning-evening differences not seen in the data. The only case where a pronounced morning-evening difference is present in the data is at the vernal equinox at low- and midlatitudes (frame 6) above 30 km. The model predicts a similar trend in this case.

The results for ice MMR show that the strong morning/evening differences in the model at the equinoxes are caused by a corresponding strong difference in simulated cloud formation. The observations sometimes show a quantitatively similar morning/evening difference in cloud formation, but involving much less abundant clouds, implying that the net impact on D/H is much reduced.

One has to take into account that the observations in the L_s-latitude bins are taken over a wide range of longitudes. Figure 15 also indicates that morning observations are taken consecutively over a wide range in L_s and latitude, and are then followed by a similar pattern for evening observations. So the comparison in Figure 19 does not consider morning and evening profiles for the same location nor for the same day. This complicates drawing any strong conclusions about diurnal variability in D/H.

5.5. Is the D/H Ratio in Water Vapor Controlled by Water Ice Clouds?

We have demonstrated that in a large majority of the observations, the modeled D/H values are consistent with observations within the reported observational variability. During the GDS and RDS, the MY34 simulation provides a clear improvement over the standard simulation in terms of the match with the data. In almost all cases the presence of ice clouds corresponds to a drop in the D/H ratio in either the observed or simulated profiles, and mostly in both. This is not trivial, as observations were taken at the terminator in rapidly changing conditions (day-night transitions). It is not strictly necessary for clouds to be present exactly at the same time and place to explain certain D/H features, as the D/H ratio is a result from the history of air parcels. Also, ice clouds may form at isolated locations in the instrument's line of sight, not necessarily corresponding to the tangent altitude where the gas-phase D/H ratio is retrieved for, and so may give a false impression. However, the main model-data biases can still be related to corresponding model-data biases for water ice clouds.

The observational data set used in this work is limited to half of a Martian year, that exhibited sometimes atypical conditions (GDS and RDS), and contains some variability and uncertainty. Also the utilized GCM has still a simple implementation of water ice clouds and fractionation. But overall, we think our analysis provides evidence that the measured D/H and its variability across time, latitude and height, can be sufficiently explained by the fractionation of water vapor on water ice clouds. On many occasions, direct co-located observations and simulations of water ice clouds provide evidence for their role—although a one-to-one correspondence is not necessary to proof such a role as the history of air parcels is also important to explain their D/H ratio.

It is at this point difficult to consolidate such a conclusion in a more quantitative way. The (relative) sparsity of the data set compared to the variety in atmospheric regimes, and its variability and uncertainty make statistical analysis complicated. To make a start, we focus on the period of the strongest change between the two simulations: the high southern latitudes during the GDS (Figure 18, frame 20). This considers the same season and latitudes, but in very different conditions, and the impact of clouds on D/H should be most apparent here. In Figure 20 we plot the model-data bias in D/H against the model-data bias for ice MMR. As both data sets are not retrieved on the same height grid, we bin the model-data differences for both in 2 km thick height layers, as before, and plot the averages together with that variability against each other, for both the standard and MY34 simulations. In the standard simulation there is excessive ice formation below ∼50 km causing a too low D/H there. In the MY34 simulation, both the ice MMR and D/H biases are improved simultaneously, providing evidence for their relationship. Given that D/H in the model can only change by fractionation upon vapor deposition, it is the improved cloud formation in the MY34 simulation that leads to an improved D/H simulation. When more extended, multi-annual data sets become available, this kind of analysis can be refined.

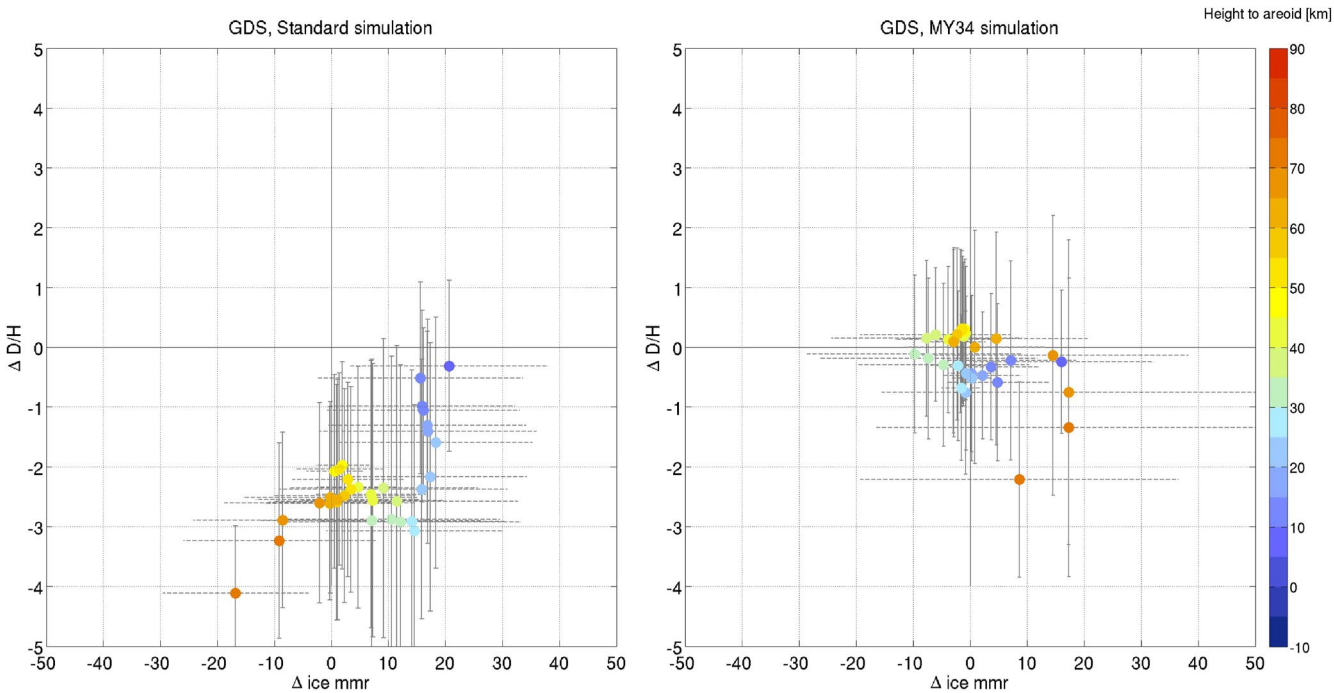

Figure 20. Model-data differences for D/H and ice mass mixing ratio (MMR) and their relation, for the standard simulation (left) and the MY34 simulation (right), both for southern latitudes (45°–90°S) during the Global Dust Storm (L_s = 195°–230°). The *y*-axes show the averaged difference in D/H (in Vienna Standard Mean Ocean Water) between model and observations in this L_s-latitude range and in 2 km thick height bins. The *x*-axes show the same for the ice MMR results (in ppmm). Error bars in both directions indicate 1σ variability. The colorscale is for height.

5.6. Rayleigh Distillation

Another way to verify that the observed D/H ratio is caused by water ice clouds is to verify if the observations follow a simple Rayleigh distillation scaling law. This law was originally derived by Rayleigh (1902) and applied by Dansgaard (1964) for fractionation by clouds, and can be written as:

$$\frac{R}{R_0} = \left(\frac{q}{q_0}\right)^{\alpha_{\mathrm{HDO}}-1}$$

with R the D/H ratio in water vapor, q the volume mixing ratio of water vapor, subscript 0 referring to reference values, and α_{HDO} the fractionation coefficient (as given by Lamb et al. (2017), see Section 2.2). From the basic theory of Rayleigh distillation, such a relation would be valid in a slow process with immediate removal of the condensate from the vapor after formation. The way D/H fractionation is implemented in our work is consistent with Rayleigh distillation, because we assume that only the instantaneous flux of deposition is at isotopic equilibrium with the gaseous phase (see Section 2.2 and Montmessin et al., 2005). The NOMAD data may provide an indication on the validity of Rayleigh distillation on Mars, applying the scaling law above.

We calculated the ratio

$$\frac{R}{R_0} \Big/ \left(\frac{q}{q_0}\right)^{\alpha_{\mathrm{HDO}}-1}$$

(we call this *Rayleigh index*) for all the observed D/H profiles, with q as in Aoki et al. (2019). As reference values (subscript 0), we used the maximum value of q and the corresponding value for R in each profile. This can only be an approximation, as the transport of water vapor and the fractionation by water ice clouds occurs in three dimensions throughout the atmosphere and not along the observed profiles. But it can be considered as a indication of the relative trends in the vertical distribution of D/H and water vapor. The fractionation coefficient α_{HDO} is temperature dependent (Section 2.2) and we calculated it using the temperature prediction from the model, for which it ranged between 1.17 (255 K) and 4 (98 K) for the considered profiles.

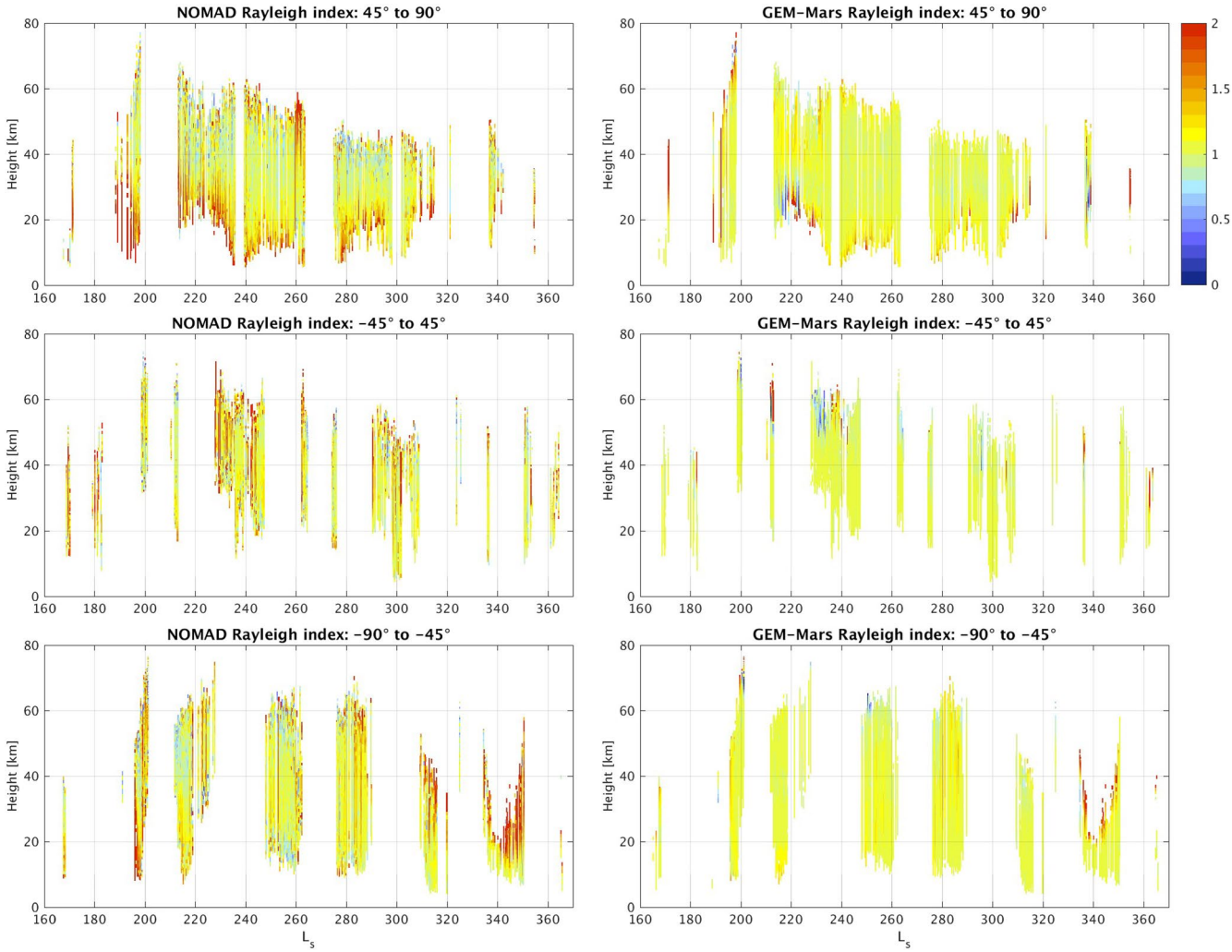

Figure 21. Rayleigh index, as defined in the text, for all NOMAD D/H profiles (left) and model simulations (right, MY34 simulation) in three wide latitude ranges.

Figure 21 shows the calculated Rayleigh index for the observations and for the model results co-located at the same profiles. In many cases, the ratio is close to unity, as can be expected for a Rayleigh distillation process. For the model results, this is expected because of the implementation of the D/H fractionation as a Rayleigh distillation process (Section 2.2). For the observations, there are some uncertainties involved, such as the large uncertainties on the D/H ratios themselves, uncertainties related to incomplete profiles due to lower- and upper cut-offs, and related to the applied (model) temperatures. Nevertheless, the similarity of the observations to the model results provides an indication that the D/H cycle on Mars can be considered as dominated by Rayleigh distillation, and hence by the (slow) fractionation by water ice clouds. However, in spite of its wealth in details, the current D/H data set remains limited in coverage, and its uncertainties cannot rule out that more sophisticated processes than Rayleigh distillation will be required in the future when a more extended, multi-annual data set will become available.

6. Conclusions

The ratio of HDO to H_2O, here addressed as D/H in water, is an important marker of the evolution of water vapor on Mars. While its understanding contributes to unraveling the long-term escape of hydrogen from, and the fate of water vapor on Mars, it was found by the NOMAD instrument on ExoMars TGO (Vandaele et al., 2019; Villanueva et al., 2021) that the ratio shows significant variations over shorter timescales, as well as with location and height. It is therefore an important diagnostic of the present-day hydrological cycle on Mars. We presented

the first direct comparisons between detailed global modeling of D/H in the Martian atmosphere and the vertically resolved observations of D/H by NOMAD. Only hydrogen isotope fractionation induced by ice formation was considered in the model. The D/H ratio was found to vary with season, latitude and height in a way similar to what was observed. The model finds that the D/H ratio in the lower atmosphere depends on the predefined ratio in the permanent north polar water ice cap, and is estimated to be 5.7 × VSMOW when the cap is initialized at 6 × VSMOW. Without any additional HDO reservoirs nor other fractionation processes, the simulations could reproduce the observations reasonably well in the time window that is currently covered by them: the second half of MY34. The simulations show that the D/H ratio is roughly constant below the zone of strongest cloud formation. The fractionation of water vapor upon cloud formation results in a strong drop of the D/H ratio with height, explaining the upper cut-off in the NOMAD observations as HDO drops below detectability.

In the time window covered by the currently available NOMAD D/H observations, a GDS and a RDS occurred. During these events the D/H from the simulation constrained by MY33 dust differed significantly from the observations. But using constraints for the MY34 dust conditions, the simulations showed that HDO is transported like H_2O to higher altitudes during the dust storms, resulting in a continuation of the lower atmospheric D/H ratio to larger heights. As a result, a good correspondence with the observations in the dust storms was obtained.

In between the storms, the aphelion and southern summer solstice seasons show stable D/H profiles with no differences between the MY33 and MY34 simulations, and on all occasions providing a good correspondence to the data. At high southern latitudes between L_s = 340°–350° low (~3 × VSMOW) D/H ratios were measured. We demonstrated that this is most likely due to a short delay of low altitude cloud formation in the south polar hood in the model. Similarly, biases in the D/H ratio in the middle atmosphere at high northern latitudes could be attributed to insufficient cloud formation in the model in those cases.

This paper illustrates, by combining unique new data and advanced global simulations, that the D/H ratio in the lower and middle atmosphere of Mars is defined by the ratio present in the permanent water ice cap (confirming the work of Montmessin et al., 2005) and that its variability is controlled by fractionation on water ice clouds assuming Rayleigh distillation. The D/H distribution is modulated by diurnally and seasonally varying cloud formation. In this data set, that covers only one half Martian year, we found no evidence of other processes or reservoirs that would have a significant impact on the D/H ratio in the lower and middle atmosphere of Mars. Moreover, the strongly changed conditions during the GDS provided a challenge for understanding the D/H ratio on Mars and to model it, and this challenge was met successfully. This provides even stronger confidence to our conclusions.

This work will have to be complemented by:

1) observations during the aphelion season, to verify if the simulations match also with the data in the season when the permanent water ice cap (the only permanent HDO reservoir considered here) undergoes significant water releases;
2) the inclusion of detailed microphysical cloud formation processes (e.g., Daerden et al., 2010; Haberle et al., 2019; Navarro et al., 2014) in the model, to refine the simulation of water ice clouds and the D/H fractionation they cause, including exploring more sophisticated fractionation processes as is done for Earth;
3) the extension of the model with HDO photolysis, and atmospheric escape processes; and additional comparisons with high altitude observations of atomic H and D.

This will then link the observations by NOMAD (and ACS) to the upper atmospheric data gathered by instruments on MAVEN (Chaffin et al., 2017, 2021; Stone et al., 2020). Eventually, a full story about water on Mars and its escape to space on the short (annual) and long timescales can be constructed.

Data Availability Statement

The results from the GEM-Mars GCM simulations used in this article are available on the BIRA-IASB data repository (https://repository.aeronomie.be/?doi=10.18758/71021067; Daerden (2021)). The NOMAD Solar Occultation D/H data set used in this work is published in Villanueva et al. (2021) and is available at https://psg.gsfc.nasa.gov in the ExoMars section. The NOMAD Solar Occultation ice MMR data set is available at the same source and on Liuzzi (2020). Dust climatologies can be found at the following link: http://www-mars.lmd.jussieu.fr/mars/dust_climatology/.

Acknowledgments
The authors thank two anonymous reviewers for constructive comments that helped to improve the paper. This work was made possible thanks to the reconstructed gridded maps of column dust optical depth from Mars Climate Sounder (MCS) observations provided by L. Montabone. The dust maps were prepared using MCS v5.3 thanks to A. Kleinböhl and D. Kass. ExoMars is a space mission of the European Space Agency (ESA) and Roscosmos. The NOMAD experiment is led by the Royal Belgian Institute for Space Aeronomy (IASB-BIRA), assisted by Co-PI teams from Spain (IAA-CSIC), Italy (INAF-IAPS), and the United Kingdom (Open University). This project acknowledges funding by the Belgian Science Policy Office (BELSPO), with the financial and contractual coordination by the ESA Prodex Office (PEA 4000103401 and 4000121493). This project has received funding from the European Union's Horizon 2020 research and innovation program (Grant Agreement No. 101004052, RoadMap project). US investigators were supported by the National Aeronautics and Space Administration, by NASA's Mars Program Office (under WBS 604796, "Participation in the TGO/NOMAD Investigation of Trace Gases on Mars."), and by NASA Award Number 80GSFC21M0002.

References

Alday, J., Trokhimovskiy, A., Irwin, P. G. J., Wilson, C. F., Montmessin, F., Lefèvre, F., et al. (2021). Isotopic fractionation of water and its photolytic products in the atmosphere of Mars. *Nature Astronomy*. https://doi.org/10.1038/s41550-021-01389-x

Alsaeed, N. R., & Jakosky, B. M. (2019). Mars water and D/H evolution from 3.3 Ga to present. *Journal of Geophysical Research: Planets*, *124*, 3344–3353. https://doi.org/10.1029/2019JE006066

Aoki, S., Nakagawa, H., Sagawa, H., Giuranna, M., Sindoni, G., Aronica, A., & Kasaba, Y. (2015). Seasonal variation of the HDO/H_2O ratio in the atmosphere of Mars at the middle of northern spring and beginning of northern summer. *Icarus*, *260*, 7–22. https://doi.org/10.1016/j.icarus.2015.06.021

Aoki, S., Vandaele, A. C., Daerden, F., Villanueva, G. L., Liuzzi, G., Thomas, I. R., et al. (2019). Water vapor vertical profiles on Mars in dust storms observed by TGO/NOMAD. *Journal of Geophysical Research: Planets*, *124*, 3482–3497. https://doi.org/10.1029/2019JE006109

Bertaux, J.-L., & Montmessin, F. (2001). Isotopic fractionation through water vapor condensation: The Deuteropause, a cold trap for deuterium in the atmosphere of Mars. *Journal of Geophysical Research*, *106*, 32897–32884. https://doi.org/10.1029/2000JE001358

Bjoraker, G. L., Mumma, M. J., & Larson, H.P. (1989). Isotopic abundance ratios for hydrogen and oxygen in the Martian atmosphere. *Bulletin of the American Astronomical Society*, *21*, 991.

Bouche, J., Coheur, P.-F., Giuranna, M., Wolkenberg, P., Nardi, L., Amoroso, M., et al. (2021). Seasonal and spatial variability of carbon monoxide (CO) in the Martian atmosphere from PFS/MEX observations. *Journal of Geophysical Research: Planets*, *126*(2). https://doi.org/10.1029/2020je006480

Chaffin, M. S., Deighan, J., Schneider, N. M., & Stewart, A. I. F. (2017). Elevated atmospheric escape of atomic hydrogen from Mars induced by high-altitude water. *Nature Geoscience*, *10*, 174–178. https://doi.org/10.1038/ngeo2887

Chaffin, M. S., Kass, D. M., Aoki, S., Fedorova, A. A., Deighan, J., Connour, K., et al. (2021). Martian water loss to space enhanced by regional dust storms. *Nature Astronomy*. https://doi.org/10.1038/s41550-021-01425-w

Christensen, P. R., Bandfield, J. L., Hamilton, V. E., Ruff, S. W., Kieffer, H. H., Titus, et al. (2001). Mars global surveyor Thermal Emission Spectrometer experiment: Investigation description and surface science results. *Journal of Geophysical Research*, *106*, 23823–23871. https://doi.org/10.1029/2000JE001370

Clarke, J. T., Mayyasi, M., Bhattacharyya, D., Schneider, N. M., Mcclintock, W. E., Deighan, J. I., et al. (2017). Variability of D and H in the Martian upper atmosphere observed with the MAVEN IUVS echelle channel. *Journal of Geophysical Research: Space Physics*, *122*, 2336–2344. https://doi.org/10.1002/2016JA023479

Conrath, B. J. (1975). Thermal structure of the Martian atmosphere during the dissipation of the dust storm of 1971. *Icarus*, *24*, 36–46. https://doi.org/10.1016/0019-1035(75)90156-6

Daerden, F. (2021). GEM-Mars GCM simulations of D/H in Mars water vapor for Daerden et al., JGR, 2021 (Data set). Royal Belgian Institute for Space Aeronomy (BIRA-IASB). https://doi.org/10.18758/71021067

Daerden, F., Neary, L., Viscardy, S., García Muñoz, A., Clancy, R. T., Smith, M. D., et al. (2019). Mars atmospheric chemistry simulations with the GEM-Mars general circulation model. *Icarus*, *326*, 197–224. https://doi.org/10.1016/j.icarus.2019.02.030

Daerden, F., Whiteway, J. A., Davy, R., Verhoeven, C., Komguem, L., Dickinson, C., et al. (2010). Simulating observed boundary layer clouds on Mars. *Geophysical Research Letters*, *37*, L04203. https://doi.org/10.1029/2009GL041523

Daerden, F., Whiteway, J. A., Neary, L., Komguem, L., Lemmon, M. T., Heavens, N. G., et al. (2015). A solar escalator on Mars: Self-lifting of dust layers by radiative heating. *Geophysical Research Letters*, *42*, 73197326. https://doi.org/10.1002/2015GL064892

Dansgaard, W. (1964). Stable isotopes in precipitation. *Tellus*, *16*(4), 436–468. https://doi.org/10.3402/tellusa.v16i4.8993

Encrenaz, T., DeWitt, C., Richter, M. J., Greathouse, T. K., Fouchet, T., Montmessin, F., et al. (2016). A map of D/H on Mars in the thermal infrared using EXES aboard SOFIA. *Astronomy and Astrophysics*, *586*, A62. https://doi.org/10.1051/0004-6361/201527018

Encrenaz, T., DeWitt, C., Richter, M. J., Greathouse, T. K., Fouchet, T., Montmessin, F., et al. (2018). New measurements of D/H on Mars using EXES aboard SOFIA. *Astronomy and Astrophysics*, *612*, A112. https://doi.org/10.1051/0004-6361/201732367

Encrenaz, T., Lellouch, E., Paubert, G., & Gulkis, S. (2001). The water vapor vertical distribution on mars from millimeter transitions of HDO and $H_2{}^{18}O$. *Planetary and Space Science*, *49*, 731. https://doi.org/10.1016/s0032-0633(01)00009-5

Encrenaz, T., Lellouch, E., Rosenqvist, J., Drossart, P., Combes, M., Billebaud, F., et al. (1991). The atmospheric composition of Mars: ISM and ground-based observational data. *Annals of Geophysics*, *9*, 797.

Fedorova, A., Bertaux, J.-L., Betsis, D., Montmessin, F., Korablev, O., Maltagliati, L., & Clarke, J. (2018). Water vapor in the middle atmosphere of Mars during the 2007 global dust storm. *Icarus*, *300*, 440–457. https://doi.org/10.1016/j.icarus.2017.09.025

Fedorova, A. A., Montmessin, F., Korablev, O., Luginin, M., Trokhimovskiy, A., Belyaev, D. A., et al. (2020). Stormy water on Mars: The distribution and saturation of atmospheric water during the dusty season. *Science*. https://doi.org/10.1126/science.aay9522

Fisher, D. A. (2007). Mars' water isotope (D/H) history in the strata of the north pole cap: Inferences about the water cycle. *Icarus*, *187*, 430–441. https://doi.org/10.1016/j.icarus.2006.10.032

Forget, F., Hourdin, F., Fournier, R., Hourdin, C., Talagrand, O., Collins, M., et al. (1999). Improved general circulation models of the Martian atmosphere from the surface to above 80 km. *Journal of Geophysical Research*, *104*(24), 24155–24175. https://doi.org/10.1029/1999je001025

Fouchet, T., & Lellouch, E. (2000). Vapor pressure isotope fractionation effects in planetary atmospheres: Application to deuterium. *Icarus*, *144*, 114–123. https://doi.org/10.1006/icar.1999.6264

Gedzelman, S. D., & Arnold, R. (1994). Modeling the isotopic composition of precipitation. *Journal of Geophysical Research*, *99*, 10455–10472. https://doi.org/10.1029/93jd03518

Giuranna, M., Wolkenberg, P., Grassi, D., Aronica, A., Aoki, S., Scaccabarozzi, D., et al. (2021). The current weather and climate of Mars: 12 years of atmospheric monitoring by the Planetary Fourier Spectrometer on Mars Express. *Icarus*, *353*, 113406. https://doi.org/10.1016/j.icarus.2019.113406

Haberle, R. M., Kahre, M. A., Hollingsworth, J. L., Montmessin, F., Wilson, R. J., Urata, R. A., et al. (2019). Documentation of the NASA/Ames legacy Mars global climate model: Simulations of the present seasonal water cycle. *Icarus*, *333*, 130–164. https://doi.org/10.1016/j.icarus.2019.03.026

Heavens, N. G., Kass, D. M., & Shirley, J. H. (2019). Dusty deep convection in the Mars year 34 planet-encircling dust event. *Journal of Geophysical Research: Planets*, *124*. https://doi.org/10.1029/2019JE006110

Heavens, N. G., Kleinböhl, A., Chaffin, M. S., Halekas, J. S., Kass, D. M., Hayne, P. O., et al. (2018). Hydrogen escape from Mars enhanced by deep convection in dust storms. *Nature Astronomy*, *2*, 126–132. https://doi.org/10.1038/s41550-017-0353-4

Hoffmann, G., Jouzel, J., & Masson, V. (2000). Stable water isotopes in atmospheric general circulation models. *Hydrological Processes*, *14*(8), 1385–1406. https://doi.org/10.1002/1099-1085(20000615)14:8<1385::aid-hyp989>3.0.co;2-1

Hu, R. (2019). Predicted diurnal variation of the deuterium to hydrogen ratio in water at the surface of Mars caused by mass exchange with the regolith. *EPSL*, *519*, 192–201. https://doi.org/10.1016/j.epsl.2019.05.017

Jakosky, B. M. (2021). Atmospheric loss to space and the history of water on Mars. *Annual Review of Earth and Planetary Sciences*, *49*, 71–93. https://doi.org/10.1146/annurev-earth-062420-052845

Jouzel, J. (1986). Isotopes in cloud physics: Multiphase and multistage condensation process. In P. Fritz & J. C. Fontes (Eds.), *Handbook of environmental isotope geochemistry, the terrestrial environment* (Vol. 2, pp. 61–112). Elsevier. https://doi.org/10.1016/b978-0-444-42225-5.50007-3

Jouzel, J., Froehlich, K., & Schotterer, U. (1997). Deuterium and oxygen-18 in present-day precipitation: Data and modelling. *Hydrological Sciences Journal*, *42*(5), 747–763. https://doi.org/10.1080/02626669709492070

Jouzel, J., & Merlivat, L. (1984). Deuterium and oxygen 18 in precipitation: Modelling of the isotopic effects during snow formation. *Journal of Geophysical Research*, *89*, 11749–11757. https://doi.org/10.1029/jd089id07p11749

Kass, D. M., Kleinböhl, A., McCleese, D. J., Schofield, J. T., & Smith, M. D. (2016). Interannual similarity in the Martian atmosphere during the dust storm season. *Geophysical Research Letters*, *43*, 6111–6118. https://doi.org/10.1002/2016GL068978

Khayat, A. S. J., Villanueva, G. L., Smith, M. D., & Guzewich, S. D. (2019). IRTF/CSHELL mapping of atmospheric HDO, H_2O and D/H on Mars during northern summer. *Icarus*, *330*, 204–216. https://doi.org/10.1016/j.icarus.2019.04.007

Kleinböhl, A., Schofield, J. T., Abdou, W. A., Irwin, P. G. J., & de Kok, R. J. (2011). A single-scattering approximation for infrared radiative transfer in limb geometry in the Martian atmosphere. *Journal of Quantitative Spectroscopy and Radiative Transfer*, *112*, 1568–1580. https://doi.org/10.1016/j.jqsrt.2011.03.006

Kleinböhl, A., Schofield, J. T., Kass, D. M., Abdou, W. A., Backus, C. R., Sen, B., et al. (2009). Mars Climate Sounder limb profile retrieval of atmospheric temperature, pressure, and dust and water ice opacity. *Journal of Geophysical Research*, *114*, E100006. https://doi.org/10.1029/2009JE003358

Korablev, O., Vandaele, A. C., Montmessin, F., Fedorova, A. A., Trokhimovskiy, A., Forget, F., et al. (2019). No detection of methane on Mars from early ExoMars Trace Gas Orbiter observations. *Nature*, *568*, 517–520. https://doi.org/10.1038/s41586-019-1096-4

Korablev, O. I., Montmessin, F., Trokhimovskiy, A., Fedorova, A. A., Shakun, A. V., Grigoriev, A. V., et al. (2018). The atmospheric chemistry suite (ACS) of three spectrometers for the ExoMars 2016 Trace Gas Orbiter. *Space Science Reviews*, *214*, 7. https://doi.org/10.1007/s11214-017-0437-6

Krasnopolsky, V. A. (2015). Variations of the HDO/H_2O ratio in the Martian atmosphere and loss of water from Mars. *Icarus*, *257*, 377–386. https://doi.org/10.1016/j.icarus.2015.05.021

Krasnopolsky, V. A., Bjoraker, G. L., Mumma, M. J., & Jennings, D. E. (1997). High-resolution spectroscopy of Mars at 3.7 and 8 mm: A sensitive search for H_2O_2, H_2CO, HCL, and CH_4, and detection of HDO. *Journal of Geophysical Research*, *102*, 6525–6534. https://doi.org/10.1029/96je03766

Krasnopolsky, V. A., & Feldman, P. D. (2001). Detection of molecular hydrogen in the atmosphere of Mars. *Science*, *294*, 1914–1917. https://doi.org/10.1126/science.1065569

Krasnopolsky, V. A., Mumma, M. J., & Gladstone, G. R. (1998). Detection of atomic deuterium in the upper atmosphere of Mars. *Science*, *280*, 1576–1580. https://doi.org/10.1126/science.280.5369.1576

Lamb, K. D., Clouser, B. W., Bolot, M., Sarkozy, L., Ebert, V., Saathoff, H., et al. (2017). Laboratory measurements of HDO/H_2O isotopic fractionation during ice deposition in simulated cirrus clouds. *Proceedings of the National Academy of Sciences*, *114*(22), 5612–5617. https://doi.org/10.1073/pnas.1618374114

Lian, Y., Richardson, M. I., Newman, C. E., Lee, C., Toigo, A. D., Mischna, M. A., & Campin, J.-M. (2012). The Ashima/MIT Mars GCM and argon in the Martian atmosphere. *Icarus*, *218*, 1043–1070. https://doi.org/10.1016/j.icarus.2012.02.012

Liuzzi, G. (2020). Data in support of Liuzzi et al. (2020). https://doi.org/10.5281/zenodo.3637564

Liuzzi, G., Villanueva, G. L., Crismani, M. M. J., Smith, M. D., Mumma, M. J., Daerden, F., et al. (2020). Strong variability of Martian water ice clouds during dust storms revealed from ExoMars Trace Gas Orbiter/NOMAD. *Journal of Geophysical Research: Planets*, *124*. https://doi.org/10.1029/2019JE006250

Marti, J., & Mauersberger, K. (1993). A survey and new measurements of ice vapor pressure at temperatures between 170 and 250 K. *Geophysical Research Letters*, *20*. https://doi.org/10.1029/93GL00105

Mauersberger, K., & Krankowsky, D. (2003). Vapor pressure above ice at temperatures below 170 K. *Geophysical Research Letters*, *30*. https://doi.org/10.1029/2002GL016183

Mayyasi, M., Clarke, J., Bhattacharyya, D., Chaufray, J. Y., Benna, M., Mahaffy, P., et al. (2019). Seasonal variability of deuterium in the upper atmosphere of Mars. *Journal of Geophysical Research: Space Physics*, *124*, 2152–2164. https://doi.org/10.1029/2018JA026244

Merlivat, L., & Nief, G. (1967). Fractionnement isotopique lors des changements d'états solide-vapeur et liquide-vapeur de l'eau à des températures inférieures à 0° C. *Tellus*, *19*(1), 122–127. https://doi.org/10.3402/tellusa.v19i1.9756

Montabone, L., Forget, F., Millour, E., Wilson, R. J., Lewis, S. R., Cantor, B., et al. (2015). Eight-year climatology of dust optical depth on Mars. *Icarus*, *251*, 65–95. https://doi.org/10.1016/j.icarus.2014.12.034

Montabone, L., Spiga, A., Kass, D. M., Kleinböhl, A., Forget, F., & Millour, E. (2020). Martian year 34 column dust climatology from Mars Climate Sounder observations: Reconstructed maps and model simulations. *Journal of Geophysical Research: Planets*. https://doi.org/10.1029/2019JE006111

Montmessin, F., Forget, F., Rannou, P., Cabane, M., & Haberle, R. M. (2004). Origin and role of water ice clouds in the Martian water cycle as inferred from a general circulation model. *Journal of Geophysical Research*, *109*, E10004. https://doi.org/10.1029/2004JE002284

Montmessin, F., Fouchet, T., & Forget, F. (2005). Modeling the annual cycle of HDO in the Martian atmosphere. *Journal of Geophysical Research*, *110*, E03006. https://doi.org/10.1029/2004je002357

Musiolik, G., Kruss, M., Demirci, T., Schrinski, B., Teiser, J., Daerden, F., et al. (2018). Saltation under Martian gravity and its influence on the global dust distribution. *Icarus*, *306*, 25–31. https://doi.org/10.1016/j.icarus.2018.01.007

Navarro, T., Madeleine, J.-B., Forget, F., Spiga, A., Millour, E., Montmessin, F., & Määttänen, A. (2014). Global climate modeling of the Martian water cycle with improved microphysics and radiatively active water ice clouds. *Journal of Geophysical Research: Planets*, *119*, 1479–1495. https://doi.org/10.1002/2013JE004550

Neary, L., & Daerden, F. (2018). The GEM-Mars general circulation model for Mars: Description and evaluation. *Icarus*, *300*, 458–476. https://doi.org/10.1016/j.icarus.2017.09.028

Neary, L., Daerden, F., Aoki, S., Whiteway, J., Clancy, R. T., Smith, M., et al. (2020). Explanation for the increase in high-altitude water on Mars observed by NOMAD during the 2018 global dust storm. *Geophysical Research Letters*, *47*, e2019GL084354. https://doi.org/10.1029/2019GL084354

Newman, C. E., de la Torre Juárez, M., Pla-García, J., Wilson, R. J., Lewis, S. R., Neary, L., et al. (2021). Multi-model meteorological and Aeolian predictions for Mars 2020 and the Jezero crater region. *Space Science Reviews*, 21720. https://doi.org/10.1007/s11214-020-00788-2

Novak, R. E., Mumma, M. J., & Villanueva, G. L. (2011). Measurement of the isotopic signatures of water on Mars; implications for studying methane. *Planetary and Space Science*, *59*, 163–168. https://doi.org/10.1016/j.pss.2010.06.017

Olsen, K. S., Forget, F., Madeleine, J.-B., Szantai, A., Audouard, J., Geminale, A., et al. (2019). Retrieval of the water ice column and physical properties of water-ice clouds in the Martian atmosphere using the OMEGA imaging spectrometer. *Icarus*, *353*, 113–229. https://doi.org/10.1016/j.icarus.2019.03.006

Owen, T., Maillard, J. P., de Bergh, C., & Lutz, B. L. (1988). Deuterium on Mars – The abundance of HDO and the value of D/H. *Science*, *240*, 1767–1770. https://doi.org/10.1126/science.240.4860.1767

Randel, W. J., Moyer, E., Park, M., Jensen, E., Bernath, P., Walker, K., & Boone, C. (2012). Global variations of HDO and HDO/H_2O ratios in the upper troposphere and lower stratosphere derived from ACE-FTS satellite measurements. *Journal of Geophysical Research*, *117*, D06303. https://doi.org/10.1029/2011JD016632

Rayleigh, L. (1902). On the distillation of binary mixtures. *The London, Edinburgh, and Dublin Philosophical Magazine and Journal of Science*, *4*(23), 521–537. https://doi.org/10.1080/14786440209462876

Rossi, L., Vals, M., Montmessin, F., Forget, F., Millour, E., Fedorova, A., et al. (2021). The effect of the Martian 2018 global dust storm on HDO as predicted by a Mars global climate model. *Geophysical Research Letters*, *48*, e2020GL090962. https://doi.org/10.1029/2020GL090962

Smith, D. E., Zuber, M. T., Solomon, S. C., Phillips, R. J., Head, J. W., Garvin, J. B., et al. (1999). The global topography of Mars and implications for surface evolution. *Science*, *284*, 1495–1503. https://doi.org/10.1126/science.284.5419.1495

Smith, M. D. (2004). Interannual variability in TES atmospheric observations of Mars during 1999–2003. *Icarus*, *167*, 148–165. https://doi.org/10.1016/j.icarus.2003.09.010

Smith, M., Daerden, F., Neary, L., & Khayat, S. (2018). The climatology of carbon monoxide and water vapor on Mars as observed by CRISM and modeled by the GEM-Mars general circulation model. *Icarus*, *301*, 117–131. https://doi.org/10.1016/j.icarus.2017.09.027

Sprague, A. L., Boynton, W. V., Kerry, K. E., Janes, D. M., Hunten, D. M., Kim, K. J., et al. (2004). Mars' South polar Ar enhancement: A tracer for south polar seasonal meridional mixing. *Science*, *306*, 1364–1367. https://doi.org/10.1126/science.1098496

Sprague, A. L., Boynton, W. V., Kerry, K. E., Janes, D. M., Kelly, N. J., Crombie, M. K., et al. (2007). Mars' atmospheric argon: Tracer for understanding Martian atmospheric circulation and dynamics. *Journal of Geophysical Research*, *112*, E03S02. https://doi.org/10.1029/2005JE002597

Stone, S. W., Yelle, R. V., Benna, M., Lo, D. Y., Elrod, M. K., & Mahaffy, P. R. (2020). Hydrogen escape from Mars is driven by seasonal and dust storm transport of water. *Science*, *370*, 824–831. https://doi.org/10.1126/science.aba5229

Vandaele, A. C., Korablev, O., Daerden, F., Aoki, S., Thomas, I. R., Altieri, F., et al. (2019). Martian dust storm impact on atmospheric H_2O and D/H observed by ExoMars Trace Gas Orbiter. *Nature*, *568*(7753), 521–525. https://doi.org/10.1038/s41586-019-1097-3

Vandaele, A. C., Lopez-Moreno, J. J., Patel, M. R., Bellucci, G., Daerden, F., Ristic, B., et al. (2018). NOMAD, an integrated suite of three spectrometers for the ExoMars Trace gas mission: Technical description, science objectives and expected performance. *Space Science Reviews*, *214*, 80. https://doi.org/10.1007/s11214-018-0517-2

Villanueva, G. L., Liuzzi, G., Crismani, M. J., Aoki, S., Vandaele, A. C., Daerden, F., et al. (2021). Water heavily fractionated as it escapes from Mars as revealed by ExoMars/NOMAD. *Science Advances*, *7*. eabc8843. https://doi.org/10.1126/sciadv.abc8843

Villanueva, G. L., Mahaffy, P. R., Flesch, G. J., Niles, P. B., Jones, J. H., Leshin, L. A., et al. (2015). Strong water isotopic anomalies in the Martian atmosphere: Probing current and ancient reservoirs. *Science*, *348*, 218. https://doi.org/10.1126/science.aaa3630

Webster, C. R., Mahaffy, P. R., Flesch, G. J., Niles, P. B., Jones, J. H., Leshin, L. A., et al. (2013). Isotope ratios of H, C, and O in CO_2 and H_2O of the Martian atmosphere. *Science*, *341*, 260. https://doi.org/10.1126/science.1237961

Whiteway, J. A., Komguem, L., Dickinson, C., Cook, C., Illnicki, M., Seabrook, J., et al. (2009). Mars water-ice clouds and precipitation. *Science*, *325*, 68. https://doi.org/10.1126/science.1172344

Yung, Y. L., Wen, J.-S., Pinto, J. P., Allen, M., Pierce, K. K., & Paulson, S. (1988). HDO in the Martian atmosphere: Implications for the abundance of crustal water. *Icarus*, *76*, 146–159. https://doi.org/10.1016/0019-1035(88)90147-9